A Proposal to PAC37: G_{Ep}/G_{Mp} with an 11 GeV electron beam

E.J. Brash (co-spokesperson), F. Benmokhtar, D. Heddle, Y. Prok
Christopher Newport University and Jefferson Lab

M.K. Jones (co-spokesperson), S. Covrig, D. Gaskell, D. Higinbotham, V.P. Kubarovsky, D. Mack, L.P. Pentchev, B. Sawatzky, G. Smith, P. Solvignon, B. Wojtsekhowski, and S. Wood
Jefferson Lab

V. Punjabi (co-spokesperson), M. Khandaker (co-spokesperson), W. Hinton
Norfolk State University

C.F. Perdrisat (co-spokesperson), M. Meziane
College of William and Mary

A.J.R. Puckett (co-spokesperson), X. Jiang
Los Alamos National Laboratory

K. Aniol, D. Margaziotis
California State University, Los Angeles

E. Tomasi
IRFU, SPhN, CEA Saclay

T. Horn
Catholic University of America

B. Hu, W. Luo
Lanzhou University

W. Boeglin, P. Markowitz, J. Reinhold
Florida International University

J.R.M. Annand, D.J. Hamilton
University of Glasgow

C. Butuceanu, M. Kohl
Hampton University

A.M. Davidenko, Yu.M. Goncharenko, Yu.M. Melnik, V.V. Mochalov, L.F. Soloviev, and A.N. Vasiliev
Institute for High Energy Physics, Protvino, Russia

N. Piskunov, D. Kirillov, I. Sitnik, J. Mushinsky, S. Basylev, V. Slepnev, I. Slepnev, G. Meshcheryakov, A. Nagaytsev, and I. Savin
Laboratory for High Energy, JINR, Dubna, Russia

Yu. Zanesvky, S. Chernenko, D. Fateev, and S. Razin
Detector Research Group

Laboratory for High Energy, JINR, Dubna, Russia

M. Mihovilovic, S. Širca
Institute Jožef Stefan

W. Bertozzi, S. Gilad
Massachussetts Institute of Technology

J. Calarco
University of New Hampshire

A. Ahmidouch, S. Danagoulian, A. Gasparian, P. Ambrozewicz
North Carolina A&T State University

L. Gan
University of North Carolina at Wilmington

A. Daniel, P. King, J. Roche
Ohio University

G.M. Huber, W. Li, Z. Papandreou
University of Regina, Canada

L. El Fassi, R. Gilman, G. Kumbartzki, R. Ransome, Y. Zhang
Rutgers University

J. Lichtenstadt, E. Piasetzky, I. Pomerantz, G. Ron
Tel Aviv University

S. Strauch
University of South Carolina

H. Baghdasaryan, D. Day, M. Shabestari, X. Zheng
University of Virginia

F.R. Wesselmann
Xavier University of Louisiana

S. Abrahamyan, A. Asaturyan, S. Mayilyan, A. Mkrtchyan, H. Mkrtchyan, A. Shahinyan, V. Tadevosyan, and H. Voskanyan
Yerevan Physics Institute, Armenia

Abstract

We propose to measure the elastic form factor ratio of the proton, G_{Ep}/G_{Mp}, up to Q^2=11 GeV^2 by polarization transfer. The proposed experiment uses exclusively instrumentation which already exists, namely the HMS and BigCal, and thus can be carried out immediately after the 11 GeV beam becomes available in Hall C. The HMS will be equiped with the existing Focal Plane Polarimeter (FPP), recently used in the GEp-III experiment. BigCal was also used in the GEp-III experiment, and both instruments performed very well during the six month duration of that experiment.

The physics interest in continuing these measurements of the form factor ratio to the largest possible Q^2 is manyfold. The data we propose to obtain will serve as direct challenges of all models of the nucleon, from phenomenological, QCD-inspired models, such as Vector Meson Dominance and Relativistic Constituent Quark Models, to more fundamental QCD lattice calculations or solutions of the Dyson-Schwinger field equations. The data will also test the limits of the Chiral Quark Soliton Model and contribute to the determination of one of the Generalized Parton Distributions.

This is an update to proposal **E12-09-101 -** G_{Ep}/G_{Mp} **with an 11 GeV electron beam**, which was conditionally approved by PAC34.

1 Rationale

Jefferson Lab proposal **E12-09-101 - G_{Ep}/G_{Mp} with an 11 GeV electron beam**, known as the GEp-IV experiment, was conditionally approved by PAC34. The aim of the experiment is to measure the ratio of the electromagnetic form factors of the proton, G_{Ep}/G_{Mp}, to as high a value of momentum transfer squared as is feasible with an 11 GeV electron beam. In the final report of PAC34, they noted the fundamental importance of measuring the electromagnetic form factors of the nucleon, and also supported the claim put forth in the proposal that the recoil polarization technique is the method-of-choice, as it is much less susceptible to two-photon exchange corrections and other systematic effects that affect the Rosenbluth separation cross section measurements. In addition, the PAC had no issues concerning the technical feasibility of the experiment.

The reason for the awarding of conditional approval status (as opposed to full approval) stemmed from their perceived overlap between the GEp-IV experiment in Hall C, and the already approved GEp-V experiment in Hall A. The latter experiment would also use the recoil polarization technique to measure the proton electromagnetic form factor ratio, and relies upon the successful implementation of the Super Bigbite Spectrometer (SBS) in Hall A. In particular, the PAC wrote:

> *"While [the proponents] consider both experiments to be complementary (high resolution and small acceptance vs. small resolution and large acceptance), the PAC is not convinced that both of them should be pursued. The PAC therefore asks the two collaborations to either come up with one common proposal or to make an extremely compelling case as to why both of them need to be done."*

Since the time of PAC34, the spokespeople of GEp-IV and GEp-V have worked together to address the issues raised by the PAC, and to develop a coordinated plan going forward. To that end, two of the GEp-IV spokespeople (Brash and Jones) were added as spokespeople to the GEp-V experiment.

From the standpoint of advancing our understanding of nucleon structure through these measurements, our common position is that the measurement of the proton form factor ratio at a Q^2 of $\sim$15 GeV^2 with an accuracy of ~ 0.1, is both necessary and attainable. Such a precise measurement at this high Q^2 is the most effective way to discriminate among the modern theoretical models of the proton and, together with other experiments at JLab at 12 GeV, will provide critical input to our understanding of nucleon structure.

Based on our previous experiments, together with detailed simulations of the equipment and detectors that are to become available following the upgrade, it is our conclusion that the GEp-V experiment, using the SBS, is the only experiment capable of achieving the above goal. However, at the same time we are also convinced that the GEp-IV experiment in Hall C using the HMS spectrometer and the existing focal plane polarimeter, together with BigCal, has a very high value, as it will provide an independent, high-precision result in what presently is an unexplored Q^2-region. In addition, the Hall C experiment would be performed without the use of substantial new funds for the experimental preparation.

Based on our experience with the GEp-III experiment, as well as numerous other recoil polarimetry experiments in Hall A, the systematic uncertainty at high Q^2 will come from

the following sources. First, and perhaps most important, is the transport of the proton spin through the magnets of the spectrometer; the issue of spin transport is one that has been studied extensively in all of the form factor ratio experiments at JLab to date, and is well understood. In addition, the relative importance of the systematic uncertainty originating from instrumental asymmetries in the proton polarimeter is expected to grow with increasing Q^2. As we have seen in the GEp-III experiment, instrumental asymmetries cancel out only to first order in the extraction of the form factor ratio. At high Q^2, where the ratio of transverse to longitudinal polarization components is very small, the effects beyond first order require special attention.

The crucial point which we wish to emphasize strongly is that the above systematic effects will be different in the GEp-IV and GEp-V experiments, and will affect the results of the experiments in different ways. Due to the enormous importance of these form factor ratio measurements to our field, it behooves us to do our utmost to ensure that these effects are fully understood, so that we can have complete confidence in the results. Thus, the two experiments should be viewed as being complementary to one another, and part of a coherent plan to obtain reliable measurements, with quantifiable systematic uncertainties, that are also of sufficiently high statistical quality to be able to discriminate between various theoretical models and approaches.

Toward this end, we have worked together to form a coordinated plan for the GEp-IV and GEp-V experiments which will allow us to evaluate and understand these systematic effects. First of all, both experiments will make a high precision measurement of the form factor ratio at a lower value of Q^2, in the region of 5-6 GeV^2. Both experiments should be able to achieve a statistical precision of ~ 0.05, which will allow us to make a detailed assessment of the systematic effects associated with the proton polarimetry and spin precession. Secondly, both experiments will make a measurement of the form-factor ratio in the region of 10-11 GeV^2 with a statistical accuracy of at least ~ 0.12. As the importance of the systematic effects are expected to be Q^2-dependent, having a comparison between GEp-IV and GEp-V at a value of Q^2 where these effects are expected to be significant is extremely valuable. Finally, in GEp-IV we will make a third measurement at a Q^2 of 8.5 GeV^2 with a statistical precision of ~ 0.1. This measurement can, in principle, be combined with the measurement at this value of Q^2 in GEp-III.

The last issue that we raise here relates to the timing of the two experiments. As of the writing of this update proposal, the funding status of the full SBS spectrometer, which is of course crucial to the completion of the GEp-V experiment, remains uncertain. While we are confident that the funding proposals which are currently being prepared will be ultimately successful, it appears that the timescale is such that completion of the GEp-V experiment will be a number of years into the future. Thus, it is our position that we should proceed with the development and completion of the GEp-IV experiment in Hall C as soon as possible. Certainly, these new measurements will generate extreme interest in the theoretical community. Moreover, we seek now full approval of GEp-IV so that we can proceed with the preparation of this experiment, including our planned upgrades of the Hall C focal plane polarimeter (which will not require JLab funds).

As a final point, we note that several approved experiments, including some proposed to this PAC, will increase the Q^2-range of the neutron form factor G_{En} very significantly. From this perspective, the new proton form factor ratio data which this experiment will provide

will be timely and will contribute significantly to the ongoing, vivacious discussion of the nucleon form factors, in particular their contribution to the determination of the Generalized Parton Distributions.

2 Introduction

In many senses, the internal structure of the nucleon is the defining problem of QCD, the fundamental theory of the strong interaction. The internal structure of the nucleon defines its mass, spin, and its interactions. The nucleon is the fundamental building block of the nucleus, and indeed it is the residual nucleon-nucleon interaction that governs all nuclear structure, in much the same way that residual interactions between atoms governs molecular structure. As such, a full and detailed quantitative understanding of the internal structure of the nucleon is a necessary precursor to extending our understanding of nuclear physics.

Based on more than a half-century of experimental and theoretical effort, we have made significant progress in our understanding of nucleon structure. At short distances, the quarks inside the nucleon are nearly unbound; this is the region of asymptotic freedom, where the quark-quark interaction is feeble. As a result, the interaction may be treated perturbatively, and the theory known as pQCD (perturbative QCD) describes a wealth of experimental data extremely well. However, at larger distances, quarks are strongly bound; this is the region of quark confinement, where QCD becomes complex, and exact quantitative calculations are exceedingly difficult.

A fundamental test of the QCD in the confinement region is the electromagnetic structure of the nucleon. In particular, measurements of the elastic electric and magnetic form factors of the proton, G_{Ep} and G_{Mp}, respectively, at large momentum transfer, Q^2, shed new light on its internal non-perturbative structure. To this point, we have relied primarily on models to attempt to describe the data. In recent years, lattice QCD has emerged as a theory which holds great promise. We note, for example, recent calculations [1, 2] of the nucleon electromagnetic form factors on the lattice; while this represents a significant step forward, much work still remains to be done before meaningful quantitative comparisons between the data and unquenched lattice QCD calculations can be made.

3 Current Status of the Experimental Data

The ratio, $R_p = \mu_p G_{Ep}/G_{Mp}$, where μ_p is the proton magnetic moment, has been measured extensively over the last several decades using two experimental techniques. In the Rosenbluth separation (or LT separation) method, one measures the angular dependence of the $e-p$ scattering cross section at a fixed value of Q^2, and obtain G_{Ep}^2 and G_{Mp}^2 separately. The results are consistent with $R_p \approx 1$ for $Q^2 < 6$ GeV^2 [3, 4, 5, 6]. In dramatic contrast, two experiments at JLab in 1998-2000, known as GEp-I and GEp-II [7, 8, 9, 10], using the polarization transfer method, where one measures R_p directly by measuring the ratio of transverse, P_t, to longitudinal, P_ℓ, polarizations of the recoiling proton, have revealed that the ratio decreases approximately linearly with increasing Q^2 over the same momentum range. The polarization transfer results are of unprecedented high precision and accuracy, due in large part to the small systematic uncertainties associated with this experimental tech-

nique, and cannot currently be reconciled with the Rosenbluth separation results. These 1998-2000 results were unexpected, and have stimulated an onslaught of theoretical papers on the subject; they are among the most often quoted results from Jefferson Lab.

One possible reason for the observed discrepancy lies in the radiative corrections which are very important for Rosenbluth cross sections, but much less so for the polarization results. With increasing Q^2, the cross section is increasingly dominated by G_{Mp}^2, and the relative contribution of G_{Ep}^2 decreases. Hence, the ϵ dependence of the radiative correction is predicted to become increasingly important to the process of extracting the form factors correctly at high Q^2. The combined effect of these two tendencies is that the cross sections contain less and less information on G_{Ep} as Q^2 increases. In contrast, what is measured in polarization transfer experiments is a ratio of cross sections, corresponding to longitudinal and transverse polarization, and both are affected similarly by radiative effects; it is this subtle cancellation effect that results in only an extremely weak dependence on radiative corrections (see Ref. [11]). Although the G_{Ep} "crisis" has still not been entirely resolved, it appears likely that a combination of more careful calculations of the standard contributions to radiative corrections, and inclusion of the previously ignored two-hard-photon contribution, might fully explain it (see, for example, Refs. [12, 13, 14, 15, 16]). The important point, though, is that the recoil polarization technique gives R_p because the signal from a small G_{Ep} is reinforced in $P_t \sim G_{Ep} \times G_{Mp}$.

The third G_{Ep}/G_{Mp} experiment, GEp-III (E-04-108), was completed in June of 2008 in Hall C [17], together with GEp-2γ and the results have been published [18]. The combined results of GEp-III and GEp-2γ extend the Q^2-range to 8.5 GeV^2. Figure 1 shows the new data at four values of Q^2: 5.17 (which was a test point used to check the spin transport procedure), two new points at 6.70 and 8.49 GeV^2, and the new point at Q^2=2.5 GeV^2 from the GEp-2γ experiment. In the GEp-2γ experiment we investigated the ϵ-dependence of G_{Ep}/G_{Mp} [19] with better than 1% statistical uncertainty, as displayed in Fig. 1. Note that in addition the results of GEp-II have recently been reanalyzed, and that variations of the ratio within statistical uncertainty have been found; the reanalyzed results for GEp-II are seen in Fig. 1 and will be published [20].

It is now clear that the quasi-linear decrease of the ratio with Q^2 discovered in the first two GEp experiments, is slowing down. The GEp-III results, together with those of GEp-I and GEp-II, suggest that the quasi-linear behavior discovered in the first two experiments is not universal (after all, a linear dependence of R_p for all Q^2 would be extremely unlikely!). The data show a systematic decrease of the slope starting at $\sim$ 4 GeV^2; that may be the expected signature of the approach to the pQCD regime, which predicts a constant ratio G_{Ep}/G_{Mp}. But the signature is soft, and this is one of several reasons why data up to 15 GeV^2 are urgently needed (see, for example, the discussion on the asymptotic behavior and F_2/F_1 in Section 4.3).

Shown in Fig. 2 are the results of the GEp-2γ experiment E-04-019 [19], which measured the ratio G_{Ep}/G_{Mp} by recoil polarization at fixed Q^2 (2.5 GeV^2), for three values of ϵ, to check the validity of the Born approximation (or to detect the contribution of the two-hard-photon process). In the Born approximation the ratio should be ϵ-independent, and the form factors should be functions of Q^2 only, as appears to be the case at the level of the current small error bars [19].

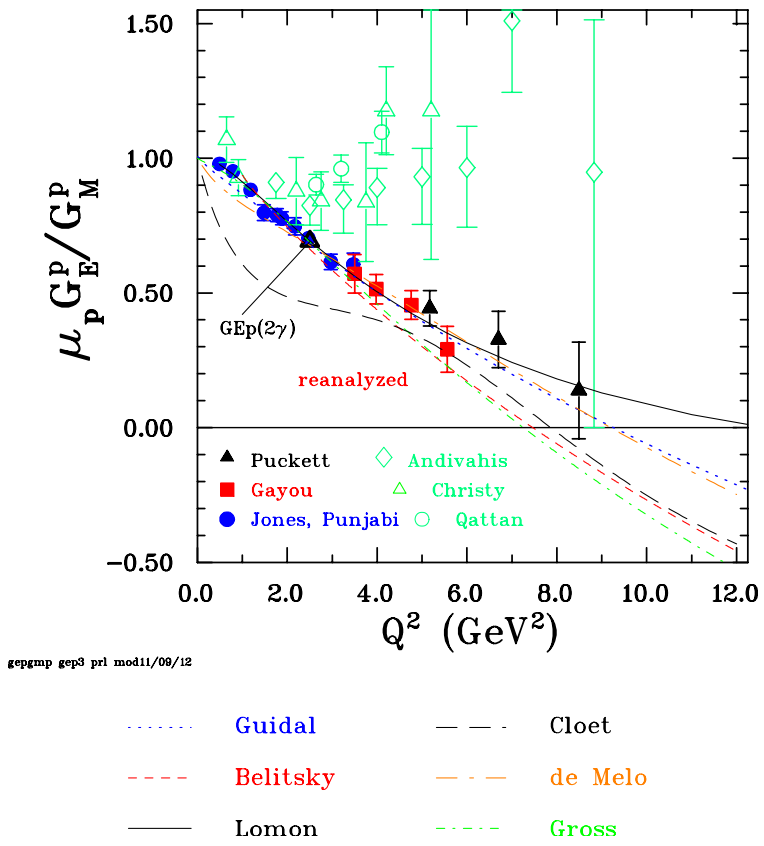

Figure 1: The recent results from GEp-III, shown as black triangles [18], together with the Hall A, 1998-2000 polarization results (blue circles and red squares) [7, 8, 10]. Also shown is the data point at 2.5 GeV^2 from the GEp-2γ experiment [19], as well as Rosenbluth cross section separation results (green symbols).

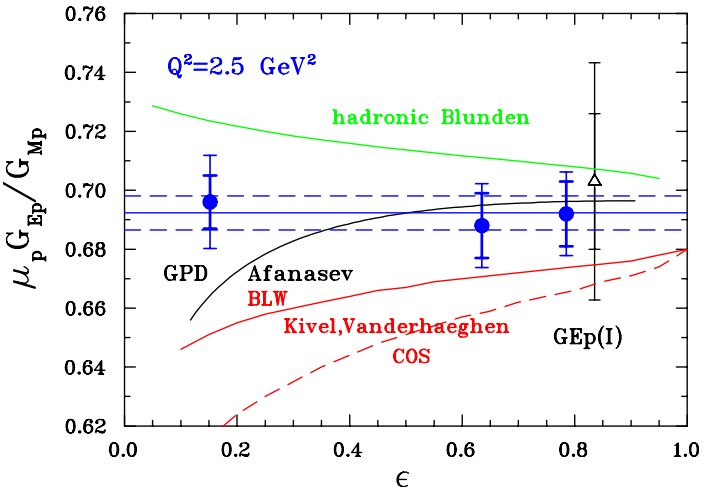

Figure 2: The preliminary results from the GEp-2γ experiment. The error bars shown are the result of combining the statistical and systematic uncertainties in quadrature.

4 Summary of Theoretical Progress

Perturbative QCD (pQCD) makes rigorous predictions when the four-momentum transfer squared, Q^2, is very large and the quarks become asymptotically free. However, it is not known precisely at what value of Q^2 pQCD may start to dominate. An exact solution to QCD in the non-perturbative regime is not possible yet, hence predicting nucleon form factors in this regime where soft scattering processes are dominant, is very difficult. As a consequence there are many complex phenomenological models trying to unravel the internal structure of the proton and neutron in this domain. The much improved quality of the form factor data from JLab has made a powerful impact on theoretical models, still the comparatively limited range of dynamic coverage of the these data results in large model uncertainties in many cases. For all these reasons precise measurements of the nucleon form factors to the highest possible Q^2 are needed.

There are several approaches to calculate nucleon form factors in the non-perturbative regime. The list includes, vector meson dominance (VMD) models, relativistic constituent quark models (rCQM), the cloudy bag model, di-quark model, the Dyson-Schwinger equation (DSE) model and more. In the VMD approach, the photon couples to the nucleon via vector mesons, whereas in QCD models the photon couples to the quarks directly. The generalized parton distribution (GPD) represents a framework within which hadrons are described in terms of quarks and gluons. Perturbative QCD predicts form factor values for large Q^2. We discuss some of these calculations in more detail here.

4.1 Vector Meson Dominance

The global features of the nucleon form factors were explained by the earliest models of vector meson dominance (VMD) models. The VMD models are a special case of more general dispersion relation fits, which provide a model-independent non-perturbative framework, to analyze the electromagnetic structure of the nucleons in both the space-like and the time-like regions.

Early VMD model calculations of form factors included the ρ and its excited states for the isovector part, and the ω and ϕ for the isoscalar part. The number of mesons involved in the interaction and the coupling constants and masses of the mesons can be varied to fit the data. The VMD fit by Iachello *et al.* [24] predicted a linear decrease of the proton G_{Ep}/G_{Mp} ratio, in basic agreement with the result from the polarization transfer experiments. Such VMD models were extended by Gari and Krümpelmann [25] to include the perturbative QCD (pQCD) scaling relations of Brodsky and Farrar [26] for the nucleon electromagnetic form factor.

In recent years, extended VMD fits which provide parametrization of all nucleon electromagnetic form factors have been obtained. An example is Lomon's fit [27], which uses $\rho(770)$, $\omega(782)$, $\phi(1020)$, and $\rho'(1450)$ mesons and contains 11 parameters. Another such recent parametrization by Bijker and Iachello [28], including $\rho(770)$, $\omega(782)$, and $\phi(1020)$ mesons, only achieves a good fit by adding a phenomenological contribution attributed to an intrinsic qqq structure (of rms radius ~ 0.34 fm) besides the vector-meson exchange terms. The pQCD scaling relations are built into this fit which has 6 free parameters which are fit to the data. Unlike the early fit of Ref. [24], the new fit of Ref. [28] gives a very good description of the neutron data at the expense of a somewhat worse fit for the proton data.

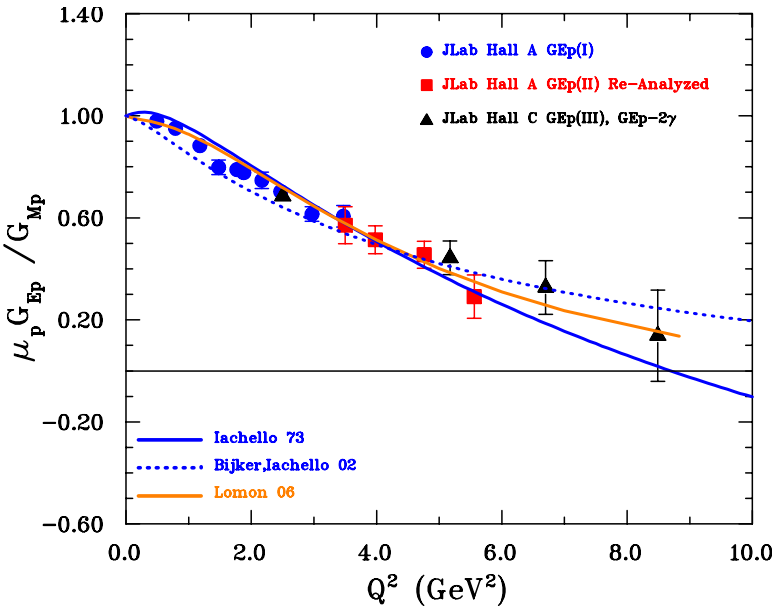

Figure 3: Comparison of vector meson dominance (VMD) model fits with the data of Ref. [7, 10, 8, 18].

Despite the relatively good fits obtained by the VMD models, such an approach is at odds with general constraints from unitarity. This problem can be repaired with the use of dispersion relations. Höhler's dispersion relation analysis [29] was extended in the mid-nineties by Mergell, Meissner, and Drechsel [30], it included the nucleon time-like form factor data [31]. The Mergell, Meissner, and Drechsel's dispersion relation analysis has been further improved by Belushkin *et al.* [32]. In addition to the 2π continuum present in the isovector spectral functions, also the $\rho\pi$ and $K\bar{K}$ continua were included as independent inputs in the isoscalar spectral functions. In Ref. [32], the 2π continuum was reevaluated using the latest experimental data for the pion form factors in the time-like region. A simultaneous fit to the world data for all four form factors in both the space-like and time-like regions was performed. The results from the fits are in very good agreement with the available experimental data.

4.2 Relativistic Constituent Quark Models

In the constituent quark model, the nucleon consists of three constituent quarks, which are thought to be valence quarks dressed with gluons and quark-antiquark pairs that are much heavier than the QCD Lagrangian quarks. All other degrees of freedom are absorbed into the masses of these quarks. The early success of the non-relativistic constituent quark model was in describing the spectrum of baryons and mesons with correct masses [33]. However, to describe the elastic form factor data in terms of constituent quarks, a relativistic description becomes crucial because the momentum transfers involved are several times the nucleon mass squared.

Chung and Coester [34] calculated electromagnetic nucleon form factors with the Poincaré-covariant relativistic constituent-quark model (rCQM). They investigated the effect of the

constituent quark masses, the anomalous magnetic moment of the quarks, and the confinement scale parameter. Their prediction is shown as a dotted line in Fig. 4. The agreement with the data over the range of Q^2 of the calculation is remarkable. In particular we note that the general trend of decreasing form factor ratio with increasing Q^2 is closely connected with the inclusion of relativistic effects.

Frank *et al.* [35] calculated G_{Ep} and G_{Mp} in the light-front constituent quark model and predicted that G_{Ep} might change sign near 5.6 GeV^2. Their predicted values is inconsistent with the current data. The calculation used the light-front nucleonic wave function of Schlumpf [36]. The light-front dynamics can be seen as a Lorentz transformation to a frame boosted to the speed of light. Under such a transformation, the spins of the constituent quarks undergo Melosh rotations. These rotations, by mixing spin states, play an important role in the calculation of the form factors. The results of their calculation are shown as the thick black solid curve in Fig. 4. The importance of this calculation lies primarily in the notion that intrinsic spin is itself a relativistic effect, and thus a comparison of the data to such calculations help us to disentangle, for example, the relativistic dynamics from other intrinsic nucleon structure effects.

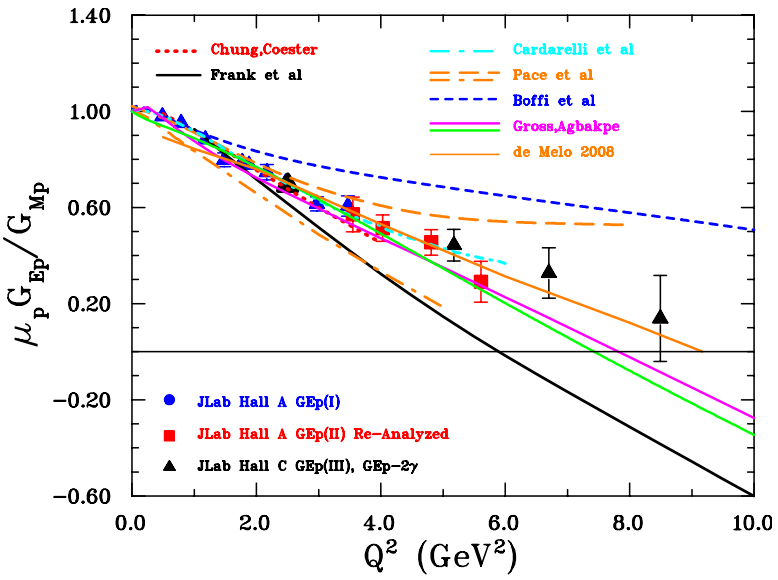

Figure 4: Comparison of constituent quark model (CQM) calculations with the data of Ref. [7, 10, 8, 18]. The curves are: dotted [34], thick solid line (black) [35], short dot-dashed [37], dot-dashed and dashed [38], short dashed [40], thin solid line (green and magenta) [42], and thin solid line (orange) [45].

Several calculations with the rCQM have been motivated specifically by the data from the JLab experiments [37, 38, 39, 40]. Cardarelli *et al.* [37] calculated the ratio with light-front dynamics and investigated the effects of SU(6) symmetry breaking. They showed that the decrease in the ratio with increasing Q^2 is due to the relativistic effects generated by Melosh rotations of the constituent quark's spin (short dot-dashed cyan curve in Fig. 4). In Ref. [38], it was pointed out that within the framework of the rCQM with the light-front formalism, an effective one-body electromagnetic current, with a proper choice of constituent quark form

factors, can give a reasonable description of pion and nucleon form factors. The results of their calculation with two different quark form factors are shown as the orange dot-dashed and dashed curves in Fig. 4. It is interesting to note that the two calculations begin to diverge significantly from one another, and from the data, with increasing Q^2. This highlights how accurate and precise data at large Q^2 can serve to further constrain such models, and thus provide a deeper understanding of the underlying structure.

De Sanctis *et al.* [39] have calculated the ratio G_{Ep}/G_{Mp} within the hypercentral constituent quark model including relativistic corrections: however, the slope of their G_{Ep}/G_{Mp} ratio is too small by a factor of ~ 2. The chiral constituent quark model based on Goldstone-boson-exchange dynamics was used by Boffi *et al.* [40] to describe the elastic electromagnetic and weak form factors. They compute these form factors in a covariant framework using the point-form approach to relativistic quantum mechanics. The results of these calculations are shown as the blue short dashed curve in Fig. 4.

Miller [41] investigated the shape of the proton by constructing a model proton wave function using Poincaré invariance and constrained by the JLab data. Interestingly, Miller puts forward the idea that a non-vanishing sum of the orbital angular momentum of the quarks of the proton is indicated by non-spherical shapes. By evaluating the rest frame ground state matrix elements of spin-dependent charge density operators, he concludes that for high momentum quarks with spins aligned either parallel or anti-parallel to the proton spin, a non-spherical shape results.

Gross and Agbakpe [42] revisited the rCQM imposing the condition that the constituent quarks become point particles as $Q^2 \to \infty$ as required by pQCD. Using a covariant spectator model which allows exact handling of all Poincaré transformations, and monopole form factors for the constituent quarks, they obtain excellent ten-parameter fits to all four nucleon form factors (shown as magenta and green solid curves in Fig. 4). They conclude that the recoil polarization data can be fitted with a spherically symmetric state of three constituent quarks.

More recently, Kvinikhidze and Miller [43] have shown that the Gross and Agbakpe model of the nucleon contains non-spherical shapes; they conclude that it is the use of the $spin-dependent$ density operator which is key to revealing these features. Finally, they point out that deviations from a spherical shape are associated physically with the motion of the spin-$\frac{1}{2}$ quarks moving relativistically within the proton. This conclusion has been contested by Gross, Ramalho and Peña [44].

A result obtained by de Melo *et al.* [45] takes into account the effect of non-valence quarks, in a light-front context. They show that the contribution of $q\overline{q}$ pairs, resulting from the Z-diagram, when added to the valence quark contribution, generates a zero crossing of the G_{Ep}/G_{Mp} ratio near 8 GeV^2 (see orange solid line in Fig. 4).

The main conclusions that we draw from the comparison of the various models to the data in Fig. 4 are:

- The models are certainly beginning to diverge from one another as Q^2 increases. Thus, new accurate and precise data at large values of Q^2 will serve to constrain these models.

- We have seen that through a comparison of the data to the various models, and through the procedure of tuning these models to the data, that we are able to gain new and important information regarding dynamical effects, as well as the underlying nucleon

structure. Moreover, the availability of accurate and precise data to as large a value of Q^2 as possible helps us to disentangle these effects from one another.

4.3 pQCD Scaling Predictions

In the pQCD approach proposed by Brodsky and collaborators [26, 46], the interaction is described as a convolution of a hard scattering amplitude and a baryon distribution amplitude. Up to leading order in $1/Q^2$, the magnetic form factor is proportional to α_s/Q^4 times slowly varying logarithmic terms, because the momentum of the virtual photon absorbed by one quark must be shared with the two other quarks through the exchange of two gluons. In lowest order the absorbed virtual photon cannot induce a quark helicity flip and consequently pQCD predicts a faster decrease of the Pauli form factor, F_{2p}, than of the Dirac form factor, F_{1p}, with increasing Q^2, by a factor Q^{-2} [26]. The expectation is then that Q^2F_{2p}/F_{1p} should become constant at very high Q^2. The experimental results, which are shown in Fig. 5 show that the new data from GEp-III suggest a decrease in the slope, hinting that the data might be approaching the pQCD limit.

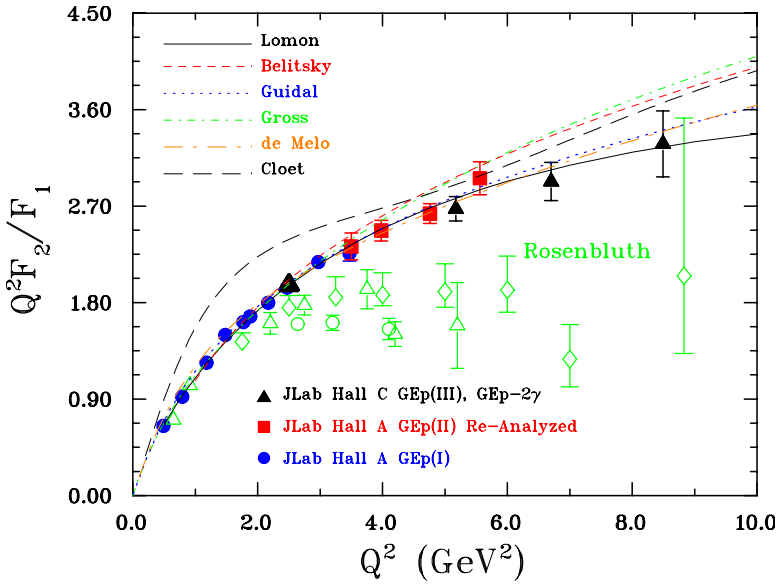

Figure 5: The ratio Q^2F_2/F_1 from various data sets. Rosenbluth separation data are from Refs. [4, 5, 6]

Further, there have been two revisions of the pQCD prediction for the large Q^2 behavior of F_2. In the first, Brodsky [47] argues that the pQCD motivated behavior of F_2 must contain an extra logarithmic term from higher twist contributions. In another approach, Belitsky, Ji, and Yuan [48] questioned the assumption of quarks moving collinearly with the proton, an underlying pQCD prediction. It has been shown in Ref. [48] that by including components in the nucleon light-cone wave functions with quark orbital angular momentum projection $l_z = 1$, one obtains the behavior $Q^2F_2/F_1 \rightarrow \ln^2(Q^2/\Lambda^2)$ at large Q^2, with Λ a non-perturbative mass scale. Choosing Λ around 0.3 GeV, Belitsky *et al.* [48] noticed that the data for Q^2F_{2p}/F_{1p} support such double-logarithmic enhancement. This is shown in

Fig. 6 where $\frac{Q^2 F_{2p}/F_{1p}}{\ln^2(Q^2/\Lambda^2)}$ is plotted, indicating approximate scaling above 2 GeV^2. The three theoretical curves shown in this figure are explained elsewhere in this document.

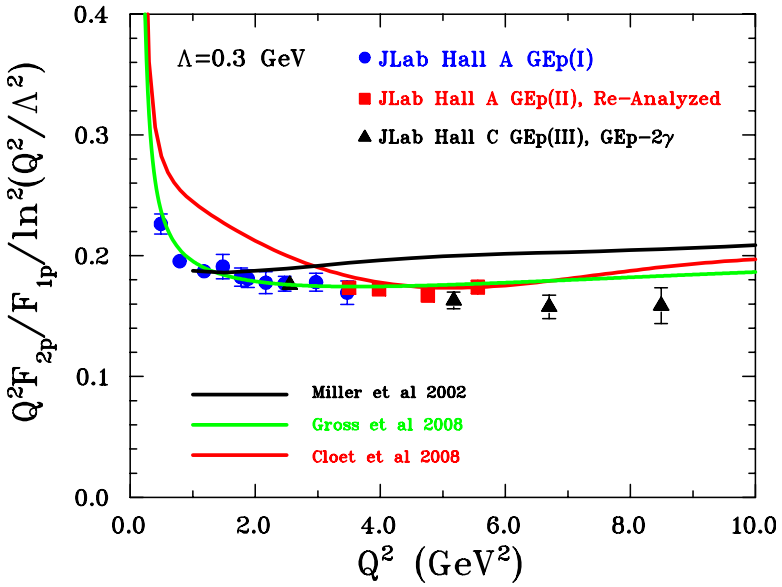

Figure 6: The ratio Q^2F_2/F_1 over $\ln^2\left(\frac{Q^2}{\Lambda^2}\right)$, compared to calculations from [35, 44, 67]

.

4.4 Generalized Parton Distributions

The generalized parton distributions (GPDs) provide a framework to describe the process of emission and re-absorption of a quark in the non-perturbative region by a hadron in exclusive reactions [49, 50, 51]; they are universal non-perturbative objects describing hard exclusive processes induced by photon and electrons or positrons. They combine together the concepts of form factors, parton densities, and distribution amplitudes, and as such serve as an extremely useful tool in studies of hadronic structure.

Precise measurements of elastic nucleon form factors provide constraints on the parametrization of the GPDs, because they are related to the first moments of the GPDs through model independent sum rule [50]. The Dirac, $F_1(t)$, and Pauli, $F_2(t)$, form factors can be calculated from GPD's H and E as:

$$F_1^q(t) = \int_{-1}^{+1} dx H^q(x,\xi,t) \qquad F_2^q(t) = \int_{-1}^{+1} dx E^q(x,\xi,t) \tag{1}$$

in which q are the quark flavors, ξ is the skewness, and t is the momentum transfer.

One of the most stringent constraints that nucleon elastic form factor data at large Q^2 can provide relates to the issue of the various contributions from quarks, gluons, and orbital angular momentum to the total angular momentum of the nucleon. A quark of flavor q in the nucleon has a total angular momentum, J^q, which is related to the GPDs H^q and E^q by the

sum rule [50] :

$$2J^q = \int_{-1}^{1} x\{H^q(x,0,0) + E^q(x,0,0)\}dx \tag{2}$$

In an early use of GPDs to describe the nucleon form factor, F_1, Radyushkin [49] parametrized the H GPD with a Gaussian form and was able to fit the existing data with only a single parameter. When precision data from the JLab experiments for F_2/F_1 up to Q^2=3.5 GeV^2 became available, Afanasev [52] extended the approach of Radyushkin and included a determination of the E GPD. This was the first attempt to extract information on the angular momentum of the valence quarks and indicated a need to measure F_2/F_1 to larger Q^2 in order to determine the x dependence of the E GPD. Using the JLab data for F_2/F_1 for the proton up to Q^2=5.6 GeV^2 and for the neutron F_2/F_1 up to Q^2=1.5 GeV^2, two theoretical groups [53, 54] fitted H and E GPDs to the existing nucleon form factor data. In Fig. 7, the proton Sachs electric and magnetic form factors are shown, and compared to the calculation of Guidal *et al.* [53] with modified Regge parametrization using three parameters. The calculation gives a good description of the available form factor data for proton in the whole Q^2 range.

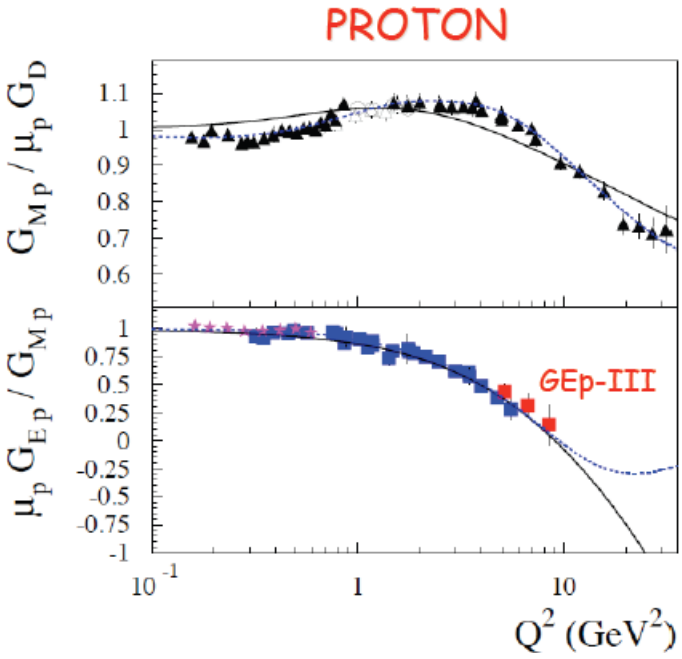

Figure 7: Proton Sachs form factors, G_{Mp}, relative to the dipole, G_D, (upper panels) and ratio of G_{Ep}/G_{Mp} (lower panel). The curves are a three parameter modified Regge parametrization.

It is possible to access the distributions of parton in the transverse plane [55, 56], and to provide a 3-dimensional picture of the nucleon [57] by a Fourier transform of the t-dependence of the GPDs. Burkhardt [55] introduced the concept that Fourier transforms of the GPDs at $\xi = 0$ describe the distribution of partons in the transverse plane. In an interesting application Belitsky *et al.* have examined the relation between quark Wigner functions and the transverse momentum dependent parton distributions and GPDs. The result make it possible to visualize quark phase space distribution, as shown in Fig. 8.

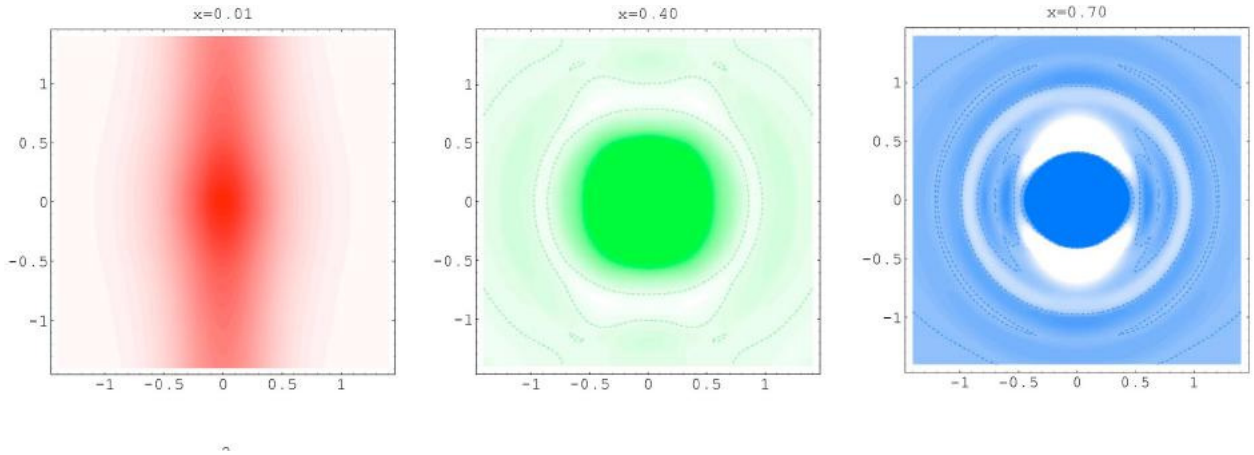

Figure 8: u quark phase space charge distribution for different Feynman x. Vertical and horizontal axes correspond to z and $\mid \vec{r}_\perp \mid$ in fm [57].

5 Charge and Magnetization Densities

Considerable progress continues to be made in understanding the relationship between momentum space form factors and position space charge and magnetization densities in the plane transverse to the momentum transfer. In particular Miller [58] has pioneered the concept of an infinite momentum frame transverse density distribution $\rho_{charge}(b)$, as two-dimensional Fourier transform of the form factor F_1, for an unpolarized proton or neutron.

$$\rho_{charge}(b) = \int \frac{QdQ}{(2\pi)} J_0(Qb) F_1(Q^2), \tag{3}$$

where J_0 is a spherical-Bessel function, and b the impact parameter. This has led to the unexpected realization that the two-dimensional transverse charge density at the center of the neutron was negative, contrary to popular wisdom, as seen in Fig. 9.

In a more recent work Miller *et al.* [59] analyzed the form factor database and obtained both charge and magnetization transverse densities using a sampling technique. The extension to the magnetization density related to F_2 has the following form:

$$\rho_2(b) = \int \frac{QdQ}{2\pi} J_0(Qb) F_2(Q)^2, \text{ leading to} \tag{4}$$

$$\rho_{mag}(b) = -b\frac{d}{db}\rho_2(b). \tag{5}$$

The results for the magnetization density are shown in Fig. 10.

One item of particular interest in the perspective of this proposal, is the global data and error analysis obtained in this work, which gives a feel of what is known about the form factors, and is illustrated in Fig. 11. The G_{Ep}/G_{Mp} results from GEp-III [18], are included in the database used for the fitting using a function which is the ratio of a polynomial over polynomial for both G_E and G_M; the pQCD behavior is forced by including a term with two

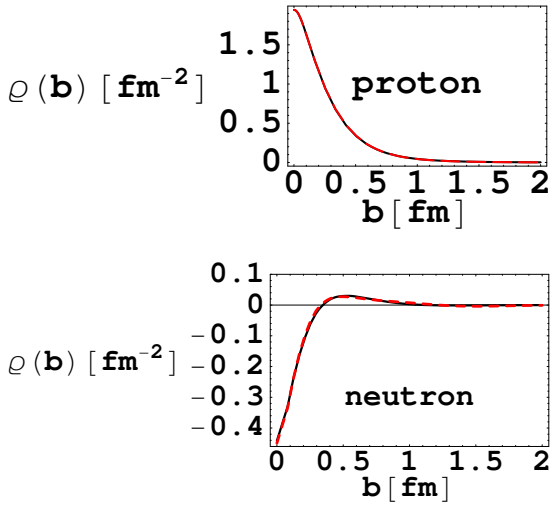

Figure 9: The transverse charge densities of the proton and neutron, $\rho_{perp}(b)$, according to Ref. [58]

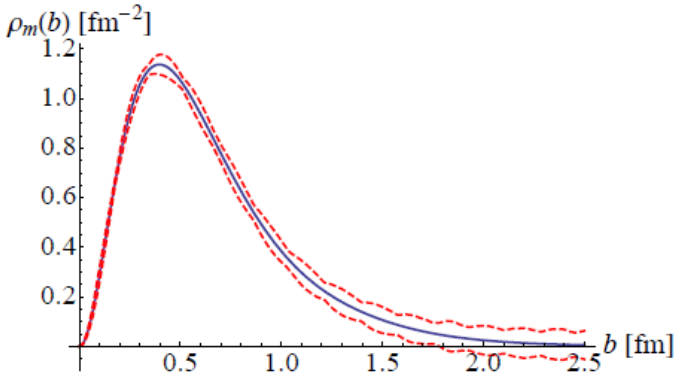

Figure 10: The true transverse magnetization distribution, ρ_{mag} according to Ref. [59].

powers of Q^2 in the denominator. Carlson and Vanderhaeghen [60] have also discussed the effect on the transverse charge distribution of a transversely polarized proton (and neutron). The resulting charge distribution for a proton polarized in the x-direction is shown in Fig. 12.

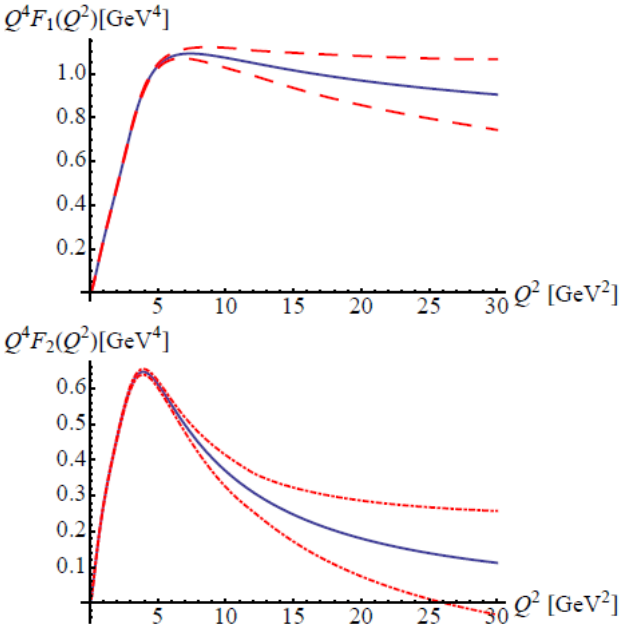

Figure 11: The fits to the form factors F_1 and F_2 multiplied by Q^4, obtained in [59].

5.1 Lattice QCD

Lattice QCD calculations of nucleon structure quantities provide *ab initio* evaluations of quantities such as the nucleon electromagnetic form factors from the underlying theory of QCD.

Lattice QCD is a discretized version of QCD formulated in terms of path integrals on a space-time lattice [61] with the only parameters, in principle, being the bare quark masses and the coupling constant. The continuum theory is obtained by extrapolating results obtained at some finite lattice spacing, a, down to a=0, requiring separate calculations at several values of a.

Typically, the u and d quark masses used are larger than the valence quark mass. This enables the inversion of the fermionic matrix, which is needed for the calculation of hadronic matrix elements, with currently available computing resources. To connect those results with reality requires extrapolation down to physical quark masses (in fact, m_q is proportional to m_π^2, and so typically calculations are evaluated as a function of m_π^2). This chiral extrapolation has only recently come down to pion mass values below 350 MeV [62, 63].

Lattice calculations for the (space-like) nucleon electromagnetic form factors require the evaluation of three-point functions, which involve two topologically different contributions: the connected and disconnected diagrams. Only the connected diagram contributes to the isovector combination of form factors $F^V = F^p - F^n$. Full QCD (un-quenched) results include both. The disconnected diagram requires a numerically more intensive calculation, and is at present neglected in most lattice studies. When taking the difference between proton and neutron electromagnetic form factors, *i.e.*, for the isovector combination of nucleon electromagnetic form factors, the disconnected contribution drops out. Figure 13 shows the m_π dependence of the isovector form factor F_1^{u-d} obtained by the LHPC collaboration [64]; the solid line represents the data; the calculation is limited to small Q^2 values.

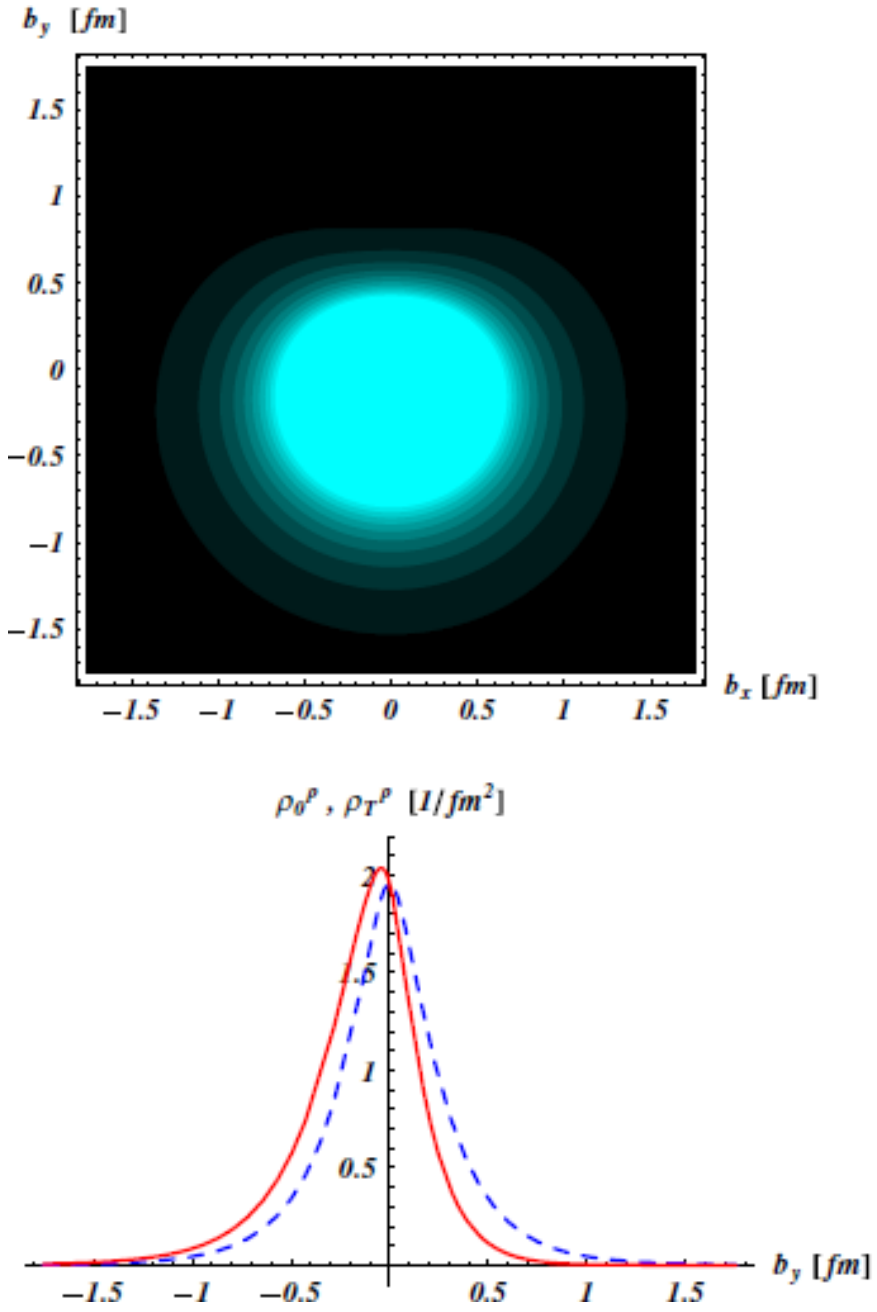

Figure 12: The transverse charge densities of a polarized proton according to Ref. [60]

.

An encouraging effort to extrapolate lattice calculation results for G_{Ep}/G_{Mp} to the physical pion mass is due to Matevosyan *et al.* [65]; they use the parameters of the light-front cloudy bag model (LFCBM) of Miller [66] to extrapolate the lattice results of the QCDSF collaboration; the results are shown in Fig. 14.

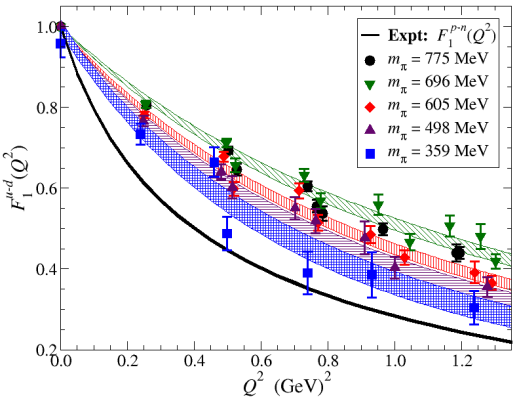

Figure 13: Isovector form factor $F_1^V = F_1^p - F_1^n$ in lattice QCD [64]

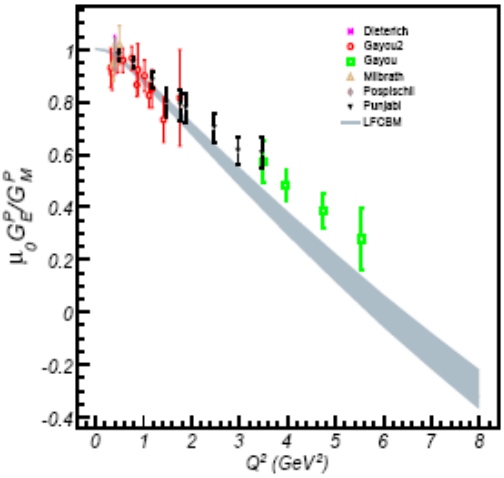

Figure 14: The physical form factor ratio obtained by extrapolating to the physical pion mass, the lattice results of the QCDSF collaboration [65, 1].

5.2 Dyson-Schwinger Equation

A different approach is illustrated by deriving solutions to the Dyson-Schwinger equations to calculate form factors, a quantum field theoretical approach to hadron structure [67]. The mechanism for mass acquisition of the QCD quark to the dressed quark mass is related to the dynamical chiral symmetry breaking; it explains the mass growth with momentum as accumulation of a gluon cloud. By solving a Poincaré covariant Faddeev equation describing two dressed quarks, Cloët and Roberts [67] obtain nucleon form factors in a model in which two quarks are always correlated, and binding results from the exchange between the di-quark and the third quark. In Ref. [67] a parameter-free Faddeev equation for the nucleon is constructed, which describes the core of dressed quarks in the nucleon. A recent result

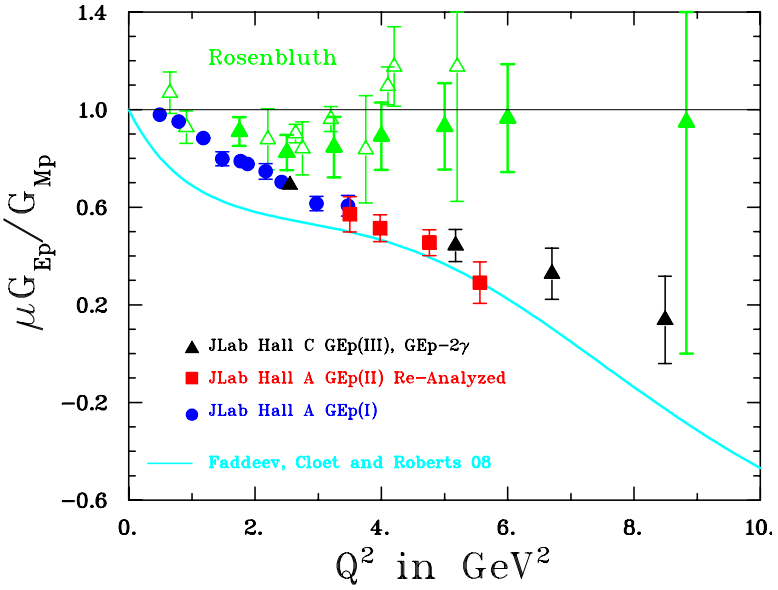

Figure 15: Nucleon form factor as solution of parameter-free Poincaré covariant Faddeev equation [67].

for $\mu_p G_{Ep}/G_{Mp}$ is shown in Fig. 15. The fact that the calculation begins to agree with the data starting around 4 GeV^2 is related to the fact that the calculation omits the pseudo-scalar meson cloud contribution.

6 The Recoil Polarization Method

The relationship between the Sachs electromagnetic form factors and the degree of polarization transfer in $^1H(\vec{e},e'\vec{p})$ scattering was first developed by Akhiezer and Rekalo [68], and later discussed in more detail by Arnold, Carlson, and Gross [69].

For single photon exchange, the transferred polarization can be written in terms of the Sachs form factors:

$$P_n = 0 \tag{6}$$

$$\pm hP_l = \pm h\left(\frac{E_e+E'_e}{M}\right)\frac{\sqrt{\tau(1+\tau)}\,G^2_{Mp}(Q^2)\,\tan^2\frac{\theta_e}{2}}{G^2_{Ep}(Q^2)+\frac{\tau}{\epsilon_\gamma}G^2_{Mp}(Q^2)} \tag{7}$$

$$\pm hP_t = \mp h\frac{2\sqrt{\tau(1+\tau)}\,G_{Ep}\,G_{Mp}\,\tan\frac{\theta_e}{2}}{G^2_{Ep}(Q^2)+\frac{\tau}{\epsilon_\gamma}G^2_{Mp}(Q^2)} \tag{8}$$

where $\tau = \frac{Q^2}{4m_p^2}$, ϵ_γ is the longitudinal virtual photon polarization, and the $\pm$ stands for the two possible orientations of the electron beam helicity.

For each Q^2, a single measurement of the azimuthal angular distribution of the proton scattered in a secondary target (described later) gives both the longitudinal and transverse

polarizations. Combining Eqs. 7 and 8 give:

$$\frac{G_{Ep}}{G_{Mp}} = -\frac{P_t}{P_l}\frac{(E_e + E'_e)}{2M}\tan\frac{\theta_e}{2}, \tag{9}$$

thus the ratio of electric to magnetic form factors of the proton is obtained directly from a simultaneous measurement of the two recoil polarization components. The kinematic factors in Eq. 9 are typically known to a precision far greater than the statistical precision of the recoil polarization components.

6.1 The Focal Plane Polarimeter

This experiment requires the re-installation of the Focal Plane Polarimeter (FPP) of the GEp-III experiment, in the focal plane area of the High Momentum Spectrometer (HMS) in Hall C. The analyzer of the FPP is divided into two blocks of CH_2, each 55 cm thick. The incoming proton trajectories are reconstructed using the HMS focal plane drift chambers to define the incident proton. Outgoing trajectories of scattered particles in either of the two analyzers are reconstructed using the FPP drift chambers, two chamber for each FPP. The original design of the chambers included three wire planes per chamber, the minimum for efficient reconstruction of the tracks. However, due to the absence of a plane with offset wires to lift accidental degeneracy, a fraction of the tracks (of order 10%) was reconstructed erroneously. We are planing to install an additional four wire planes, one per chamber, and expect this to improve the efficiency of the FPPs by about 10%. In Fig. 16 we show the double FPP installed in the detector hut of the HMS during GEp-III.

The FPP has been designed as a unit in a sturdy frame, to facilitate its installation and removal. All required infrastructures for this installation are still available.

For the purposes of determining the polarimeter Coefficient of Merit (COM) defined as $COM = \int \eta(\vartheta_{fpp})A_y^2(\vartheta_{fpp})$, where $\eta(\vartheta_{fpp})$ is the fraction of incident protons scattering at given polar angle ϑ_{fpp} in the FPP, for calculating projected uncertainties, the differential scattering fraction have been estimated from a full GEANT3-based simulation of the polarimeter. The data of GEp-III showed these predictions to be reasonably accurate.

In Fig. 17 we show the currently available maximum analyzing power values, A_y^{max}, from the previous JLab experiments, as well as from measurements at Dubna [71] for CH_2, and at Saclay [72] and Moscow [73] for Carbon. The black circles are the values of A_y obtained in GEp-III. We have assumed that the difference with previous results, which goes in the right direction, is due to the stricter selection of single-track events enforced in GEp-III; such selections could not be accomplished in GEp-II or in the Dubna calibration because of the multiplexed nature of the wire chamber readouts in these two experiments. A combined analysis [71] of the carbon and CH_2 data has showed that empirically, the maximum analyzing power is proportional to $1/p$, the inverse of the proton momentum over a large range of proton momenta. It is also true that A_y^{max} occurs at a fixed value of the transverse momentum transfer, $p_T = p\sin(\vartheta_{fpp}) \simeq 0.3$ GeV/c. The GEp-III results still satisfy the proportionality of A_y^{max} to $1/p$, albeit with a smaller slope, an advantage. Moreover, the shape of the analyzing power curve as a function of transverse momentum (which is proportional to the polar angle, ϑ_{fpp}) is largely independent of momentum, as well. The scaling observed implies that when represented as a function of p_T all values of pA_y are on one unique curve, thus providing excellent prediction of the polarimeter performance to values of p not yet explored. We

have extrapolated the linear fit to the A_y^{max} data into the region of proton momenta which correspond to this experiment, and have used these values to estimate the average analyzing powers. We note that this is probably a somewhat *pessimistic* scenario, as it is quite likely that the maximum analyzing power will be larger than the $1/p$ extrapolation because of the increase of the number of wire planes that we intend to install for this experiment. A second calibration experiment up to 7 GeV/c is approved at the Dubna Nuclotron; it will take place prior to the running of GEp-IV.

Figure 16: The double Focal Plane Polarimeter installed in the HMS detector hut, during the 2007-2008 GEp-III experiment. For GEp-IV it will be re-installed exactly as before.

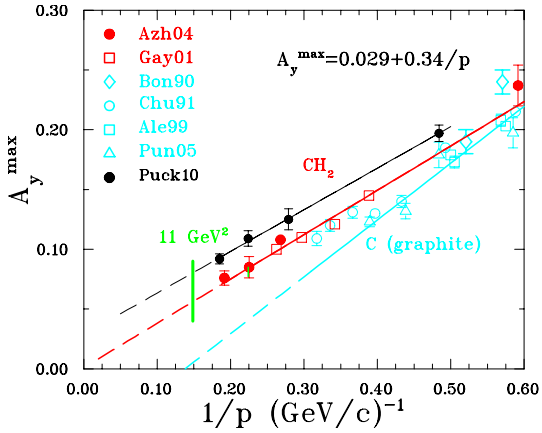

Figure 17: Maximum carbon/CH_2 analyzing power data. The filled black circles show the A_y^{max} values obtained from the GEp-III data.

In Fig. 18 we show the azimuthal asymmetry distribution helicity difference for the 8.5 GeV^2 data point of GEp-III. As the amplitude of the modulation is determined by the beam polarization, the longitudinal polarization component P_ℓ corrected for the spin precession χ and the average analyzing power A_y^{aver}: $P_e P_\ell \sin\chi A_y^{aver}$, it remains similar for increasing Q^2; P_ℓ is defined by the ϵ-value when R_p is small.

In Fig. 19 the independence of the ratio R_p versus the target vertical- and horizontal slopes is demonstrated with the high statistics data of the GEp-2γ experiment. The spin precession due to the presence of the quadrupoles in the HMS, very visible when a simple dipole calculation of the precession is done, disappears when the spin transport code COSY is used, a measure of the quality of the field description achieved with this code. These results are qualitatively essentially Q^2-independent.

6.2 Spin Precession

In all recoil polarization experiments, elastic ep events are identified using coincident detection of both electron and proton. In this experiment, the electron will be detected using a lead-glass detector array (as was the case in the completed GEp-III (JLab E04-108) experiment in Hall C), and the proton will be detected with the High Momentum Spectrometer (HMS). As the proton travels through the HMS, its spin precesses due to the interaction of

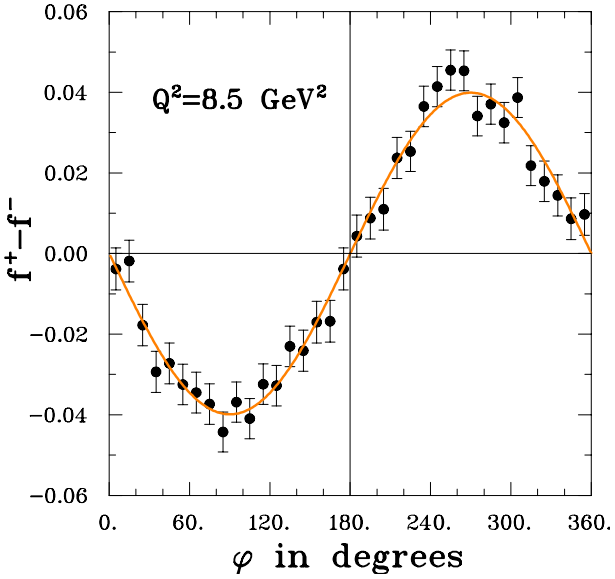

Figure 18: The basic data of a polarization transfer experiment: the azimuthal asymmetry difference for beam helicity $+$ and $-$, summing the events of the two FPPs; example of the Q^2=8.5 GeV^2 data point from GEp-III.

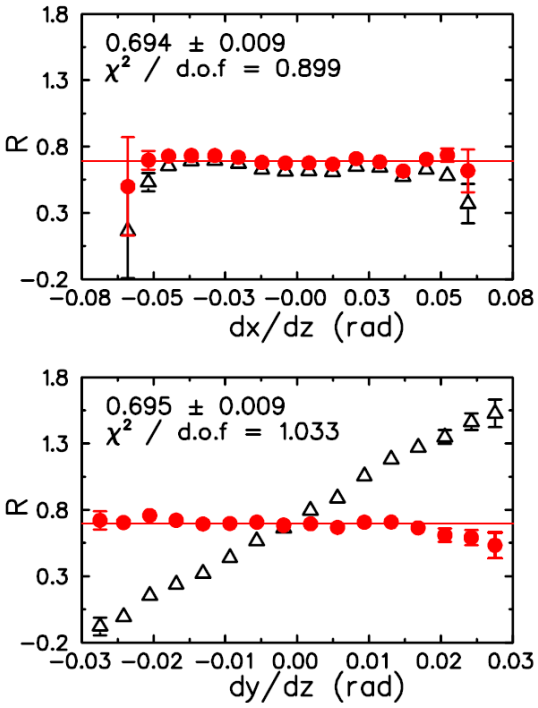

Figure 19: The ratio R_p versus the dispersive dx/dz (vertical angle) and non-dispersive dy/dz (horizontal angle) slopes for Q^2=2.5 GeV^2 and ϵ =0.152 of the GEp-2γ experiment, using the dipole approximation (no quadrupole, open triangles) and the COSY model (filled circles).

the magnetic moment of the proton with the magnetic field of the HMS, which consists of a series of three quadrupole magnets, followed by a vertical-bend dipole magnet with a 25° bend for the central ray.

The proton polarization at the spectrometer focal plane is related to its polarization at the target by a spin matrix:

$$\begin{pmatrix} \mathbf{P_n^{fp}} \\ \mathbf{P_t^{fp}} \\ P_l^{fp} \end{pmatrix} = \begin{pmatrix} S_{nn} & \mathbf{S_{nt}} & \mathbf{S_{nl}} \\ S_{tn} & \mathbf{S_{tt}} & \mathbf{S_{tl}} \\ S_{ln} & S_{lt} & S_{ll} \end{pmatrix} \begin{pmatrix} P_n^{tar} \\ \mathbf{P_t^{tar}} \\ \mathbf{P_l^{tar}} \end{pmatrix}$$

The focal plane polarimeter measures only the transverse and normal, P_t^{fp} and P_n^{fp}, components of the proton polarization. The spin matrix is calculated using a model of the spectrometer with the differential-algebra-based transport code COSY. Details are given in Ref. [10] regarding the method for extracting the target polarizations from knowledge of the spin matrix and measurement of the $N^{\pm}(\theta, \phi)$ distributions. For a simple QQQD magnetic spectrometer such as the HMS, the "off-diagonal" spin matrix elements S_{nt} and S_{tl} are almost zero when averaged over the acceptance, while the "diagonal" elements are $S_{tt} \approx 1$ and $S_{nl} \approx -\sin\chi_\theta$, where $\chi_\theta = \gamma\kappa_p\theta_{bend}$ is the precession angle of the proton spin relative to

its trajectory in the dipole, γ is the proton's boost factor, κ_p is the proton's anomalous magnetic moment, and θ_{bend} is the trajectory bend angle in the dipole. In first approximation, the error in the extracted value of P_l^{tar} is magnified by a factor of $1/\sin\chi_\theta$ due to the attendant reduction in the size of the measured focal plane asymmetry. In practice, since a wide range of χ is populated by elastic events at the focal plane, the error magnification on P_l calculated at the central value of χ is significantly overestimated for $\sin\chi$ near zero and slightly underestimated for $\sin\chi$ near 1. The value of χ_θ is determined by the proton momentum and the bend angle of the spectrometer, and in general, the optimal Q^2 for a given magnetic setup is that for which $|\sin\chi_\theta| \approx 1$.

In the simple dipole approximation, the relevant matrix elements are $S_{nl}^{dipole} = -\sin\chi_\theta$, $S_{tl}^{dipole} = 0$, $S_{tt}^{dipole} = 1$, $S_{nt}^{dipole} = 0$. In reality, the quadrupoles cause additional precession in the non-dispersive (horizontal) plane. While these quadrupole corrections tend to cancel when averaged over the spectrometer acceptance, they cannot generally be neglected, for two reasons. First, since the precession in the non-dispersive plane mixes P_t and P_l, the form factor ratio is highly sensitive to the matrix element S_{tl}. Second, since the scattering cross section depends strongly on the proton scattering angle θ_p, the distribution of ϕ_{tar}, the proton trajectory angle in the non-dispersive plane, is generally highly asymmetric, so that the acceptance-averaged precession effects do not exactly cancel. In practice, these two experimental facts lead to sizeable corrections in the full spin transport calculation relative to the simple dipole approximation.

Nonetheless, the spin transport properties of the Hall C HMS are very well understood. The HMS is an excellent device from the point of view of spin precession, because of its simple QQQD structure, which greatly simplifies the calculation of the spin transport matrix. In fact, an excellent approximation to the relevant elements of the spin transport matrix of the HMS including dispersive and non-dispersive plane precessions is given by the product of simple rotations by angles $\chi_\phi = \gamma\kappa_p(\phi_{fp} - \phi_{tar})$ in the non-dispersive plane followed by a rotation by angle χ_θ in the dispersive plane (as in the dipole approximation). The relevant matrix elements in this "geometric" approximation are $S_{tt} = \cos\chi_\phi$, $S_{tl} = \sin\chi_\phi$, $S_{nt} = \sin\chi_\phi\sin\chi_\theta$ and $S_{nl} = -\cos\chi_\phi\sin\chi_\theta$. The excellent agreement between this simple "second-order" approximation and the full COSY calculation allows for detailed and rapid evaluation of systematic uncertainties.

The dominant systematic uncertainty in the determination of G_{Ep}/G_{Mp} comes from the uncertainty in the non-dispersive precession angle χ_ϕ, or equivalently, the trajectory bend angle in the non-dispersive plane $\phi_{bend} = \phi_{fp} - \phi_{tar}$, due to unknown misalignments of the HMS quadrupoles. Dedicated optics studies performed during the GEp-III experiment showed that the uncertainty $\Delta\phi_{bend}$ was no greater than 0.5 mrad. Since the uncertainty in P_t/P_l, and therefore in R, is directly proportional to $\Delta\phi_{bend}$, it is important to keep it as small as possible. At the level achieved in the analysis of GEp-III, the dominant non-dispersive precession uncertainty in R would be $\Delta R = 0.015$ at Q^2 = 6 GeV^2, $\Delta R = 0.024$ at Q^2 = 8.5 GeV^2 and $\Delta R = 0.035$ at Q^2 = 11 GeV^2 [1]. A carefully redesigned program of optical studies with enhanced sensitivity to $\Delta\phi_{bend}$ will reduce this uncertainty even further, but even at the level of understanding already achieved for the HMS, the systematic uncertainty will

[1]Even though γ is higher in GEp-IV at Q^2=11 GeV^2 than in GEp-III at the highest Q^2, the kinematic magnification of the precession uncertainty is lower since we are at $\epsilon = 0.7$ compared to $\epsilon \approx 0.24$ in GEp-III. For the proposed measurement at Q^2=8.5 GeV^2, we have $\epsilon = 0.83$.

be quite small relative to the statistical uncertainty.

7 The Experiment

This experiment will use the High Momentum Spectrometer (HMS) in Hall C to detect the recoiling proton, and BigCal to detect the scattered electron. The focal plane in the HMS will be equipped with the Focal Plane Polarimeter (FPP) that was also installed in the HMS during the GEp-III experiment. We have assumed the existence of a 30 cm long liquid hydrogen target, which of course can and will be used for a multitude of experiments in Hall C in the 12 GeV era. Therefore, this experiment requires no new equipment beyond the base equipment planned for the Hall C 12 GeV upgrade.

7.1 The High Momentum Spectrometer

The HMS bends charged particles in the vertical plane; it consists of three quadrupoles, followed by a vertical bend dipole magnet, operated in a point-to-point tune. Its angular acceptance is approximately 6.7 msr. The angular resolution is approximately 1.0 mrad in both the in-plane and out-of-plane directions, and the momentum resolution is approximately 0.1%. These momentum and angular resolutions are perfectly adequate for this experiment. The highest momentum accepted by the HMS is 7.4 GeV/c, corresponding to $Q^2 \approx 12$ GeV^2; the vertical bend angle of the HMS is 25°.

As described in the previous section, favorable precession angles are crucial to obtain the ratio G_{Ep}/G_{Mp} with small uncertainty. For the highest Q^2 values considered for this proposal (10.5 GeV^2 $< Q^2 <$ 11.5 GeV^2), the central precession angle χ_θ ranges from $312^\circ \leq \chi_\theta \leq 338^\circ$, or in terms of the central value of $\sin\chi_\theta$, $-0.74 \leq \sin\chi_\theta \leq -0.38$, with $\sin\chi_\theta = -0.58$ at Q^2 = 11 GeV^2. While the optimal Q^2 for the HMS in terms of χ is $Q^2 \approx 9$ GeV^2, the value of χ at Q^2 = 11 GeV^2 is more than adequate to perform a measurement to the needed precision, and maximizing the physics potential of the proposal requires us to measure to the maximum feasible Q^2. Given the tradeoff between the physics impact of measuring to higher Q^2, the steep drop in rate with increasing Q^2, and the increasingly unfavorable precession angles for Q^2 from 9 GeV^2 up to the maximum HMS central momentum, Q^2 =11 GeV^2 is the most logical choice. The projected uncertainty for a given beam time varies only slowly between $10.5 \leq Q^2 \leq 11.5$ GeV^2.

As in the GEp-III experiment, the HMS focal plane drift chambers will serve the dual purpose of measuring the proton kinematics and defining the proton's incident trajectory for the measurement of the angular distribution of the secondary scattering in CH_2. The standard "S1" scintillator hodoscopes will provide the trigger for the proton arm. In the GEp-III experiment, the trigger rate was reduced by installing an added plane of scintillators "S0" upstream of the HMS focal plane drift chambers and requiring a coincidence between S0 and S1. The purpose of S0 was to reduce the acceptance to the envelope of elastically scattered events and to provide added lever arm between scintillators in the trigger in order to trigger only on good tracks passing through both of the HMS drift chambers. The single-arm trigger rates of the HMS and BigCal required this addition in order to keep the accidental rates manageable. The installation of S0, however, had the drawback of degrading the resolution of the reconstructed proton angles at the target due to the introduction of ≈ 1 mrad of

multiple scattering before the measurement of the proton track. An alternative solution is to install smaller-area scintillators between the first and second HMS drift chambers, near the optical focal point of the spectrometer, where the envelope of elastic events is comparatively smaller. Experience during the Wide-Angle Compton Scattering experiment which ran consecutively with GEp-III, shows that this option reduces the magnification of the resolution in the reconstructed kinematics due to the extra multiple scattering, since no extra multiple scattering occurs before the first drift chamber and the distance from the extra scintillators to the second drift chamber is smaller.

In the GEp-III experiment, the installation of S0 upstream of the drift chambers to reduce the trigger rate was required mainly for the kinematics at Q^2 = 8.5 GeV^2 and for the lowest ϵ kinematics in the GEp-2γ experiment at Q^2 = 2.5 GeV^2. Both of these kinematics featured large electron scattering angles θ_e and very forward proton angles $\theta_p = 11.6^\circ$ at Q^2 = 8.5 GeV^2 and $\theta_p = 14.5^\circ$ at Q^2 = 2.5 GeV^2, $\epsilon = 0.15$. Furthermore, both of these kinematics required very large solid angles ($100+$ msr) for the electron arm, increasing the background rate of the BigCal detector.

The singles rate for the HMS is a complicated function of the beam energy E_{beam}, the central momentum setting p_0, and the spectrometer angle θ_{HMS}, but as a general rule, the rate decreases as θ_{HMS} is increased for fixed E_{beam} and p_0, as E_{beam} is increased for fixed p_0 and θ_{HMS}, and as p_0 is increased for fixed E_{beam} and θ_{HMS}. Because p_p, θ_p and E_{beam} are always correlated in elastic scattering, it is not possible to directly predict the HMS singles rate for the proposed kinematics from the observed rates in the GEp-III experiment. However, our experience suggests that singles rates for the logical combination of S1 signals used in the custom trigger of the GEp-III and GEp-2γ experiments do not vary strongly as a function of angle, beam energy, and central momentum. Scaled to a beam current of 75 μA and a liquid hydrogen target thickness of 30 cm at the nominal operating point, the S1 trigger rates observed during the GEp-III/GEp-2γ, experiments range from 20-100 kHz. The maximum rate capability of the data acquisition system in Hall C is optimistically 5 kHz, and the practical safe limit for reasons of computer deadtime is 1-2 kHz. Therefore, the coincidence trigger with the calorimeter must reduce the rate by a factor of 10-100 depending on what the singles rates will actually be.

The singles rate in the calorimeter is determined by four variables: the beam energy, the calorimeter angle, the calorimeter distance (relative to its size) and the calorimeter trigger threshold. In the proposed kinematics, the scattered electron energy will be E'_e = 5.6 GeV for Q^2 = 6 GeV^2, E_{beam} = 8.8 GeV, E'_e = 6.5 GeV for Q^2 = 8.5 GeV^2, E_{beam} = 11 GeV, and E'_e = 5.1 GeV for Q^2 = 11 GeV^2, E_{beam}=11 GeV. We will apply a high threshold of approximately half the elastic ep energy; ***i.e.***, 2.8 GeV (Q^2=6), 3.2 GeV (Q^2=8.5) or 2.5 GeV (Q^2=11) to suppress the trigger rate from low-energy and inelastic backgrounds. The required electron solid angle for acceptance matching in this experiment is significantly smaller than in GEp-III, since $\theta_e = 25.5^\circ$, 19.9° and 20.1° and ϵ =0.70, 0.83 and 0.85 for Q^2 = 11, 8.5 and 6 GeV^2, respectively. The corresponding electron solid angle is approximately 1.8 times the size of the HMS acceptance for Q^2 = 11 GeV^2 and is smaller than the HMS acceptance for Q^2 = 8.5 and 6 GeV^2. Therefore, we generally expect the calorimeter trigger rates to be lower than experienced in the worst case of GEp-III at Q^2 = 8.5 GeV^2, where the solid angle of BigCal was 143 msr. Assuming a coincidence timing window of $\pm$30 ns, a HMS S1 rate of 30 kHz, and a calorimeter trigger rate of 300 kHz, the accidental coincidence rate would

be roughly 540 Hz, which is close to the safe limit from the point of view of DAQ deadtime. The corresponding expected signal rate is roughly 60/14/5 Hz for Q^2 = 6/8.5/11 GeV^2. After applying all elastic event selection cuts in the offline analysis, and applying a loose cut to the true coincidence peak in the correlation of the HMS and calorimeter time signals, the contamination from random coincidences will be at the 10^{-3} level or lower, which is certainly safe from the point of view of the data analysis.

Although we have reason to expect that the HMS trigger rate with S1 only may in fact be lower than the 10-100 kHz range found in GEp-III/GEp-2γ, even if the accidental coincidence rate cannot be kept within the limits of the DAQ system with reasonably low deadtime by tightening the coincidence time window or increasing the calorimeter threshold (50% of the elastic ep energy is the safe limit from the point of view of efficiency), we will easily reduce the rate by installing extra scintillators in the trigger as in the GEp-III experiment. Though ideally no scintillators would be placed upstream of the HMS drift chambers in order to maximally exploit the resolution of the HMS for the selection of elastic events, if this is required in practice, it presents no significant difficulty for the data analysis, as described below.

The dominant source of inelastic background in these experiments is hard-bremsstrahlung induced π^0 photoproduction, $\gamma + p \rightarrow \pi^0 + p$, with one or both π^0 decay photons detected in the calorimeter. Because our lead-glass calorimeter cannot distinguish between electrons and photons of similar energies, this background can only be separated from elastic ep using two-body kinematic correlations between the calorimeter and the HMS. Near endpoint, the kinematics of the proton in this background process overlap with elastic kinematics within the resolution of the HMS, and cannot be separated on the basis of the proton angle-momentum correlation alone. Our ability to suppress this background relies principally on the correlation between the position of the detected electron at the calorimeter and its expected position calculated from the measured kinematics of the proton assuming elastic scattering. The isotropic angular distribution (in the π^0 rest frame) of the photons from π^0 decay tends to destroy this correlation for the background. After applying this cut, an additional cut on the proton angle-momentum correlation suppresses π^0 events in the inelastic region produced by photons at energies below the full beam energy, and a loose cut on the calorimeter missing energy can provide some additional suppression of the background. However, there is an essentially irreducible number of events with photon energies near the full beam energy and with a photon detected at the calorimeter inside the elastic peak region where the broad "hill" of π^0 photons overlaps the sharp peak from elastic ep events. Although the π^0 decay photons have definitively lower energies than elastic ep electrons, the relatively poor energy resolution of lead-glass calorimeters and the fact that electron and photon showers of similar energies give indistinguishable signals in lead-glass does not allow us to efficiently discriminate between the two reactions based on the measured calorimeter energy. In fact, there is no way to completely eliminate this background without adding extra detectors and/or magnets to the setup, and as such, the experiment is at the mercy of the relative rate between $ep \rightarrow ep$ and $\gamma p \rightarrow \pi^0 p$ being favorable enough that the combination of the angular and momentum resolution of the HMS and the coordinate resolution of the calorimeter is sufficient to suppress it to an acceptable level. As an extreme example, we show the background situation at Q^2= 8.5 GeV^2 observed in the GEp-III experiment in Fig. 20, for which the irreducible background amounted to 6% of all events passing the final cuts.

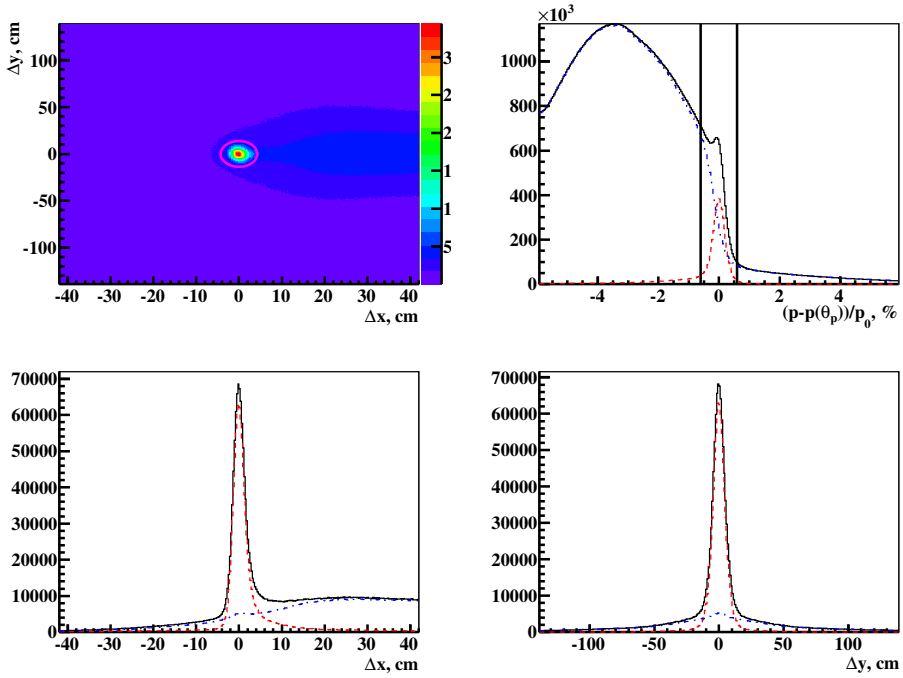

Figure 20: Effect of cuts in GEp-III, Q^2 = 8.5 GeV^2. Top left: the correlation between horizontal Δx and vertical Δy differences between expected and measured calorimeter coordinates. The elastic peak is obviously at $(0, 0)$. The ellipse shows the cut used in the analysis. Top right: difference between measured proton momentum and expected momentum from the measured proton angle, expressed as a percentage of the HMS central momentum, for all events (black solid), events passing elliptical cut (red dashed) and events failing the cut (blue dot-dash). Vertical lines indicate the cut applied to this variable. Bottom left: projection of calorimeter coordinate difference on the Δx axis for all events (black solid), events passing the $p - p(\theta)$ cut (red dashed) and events failing this cut (blue dot-dashed). Bottom right: projection of calorimeter coordinate difference on the Δy axis.

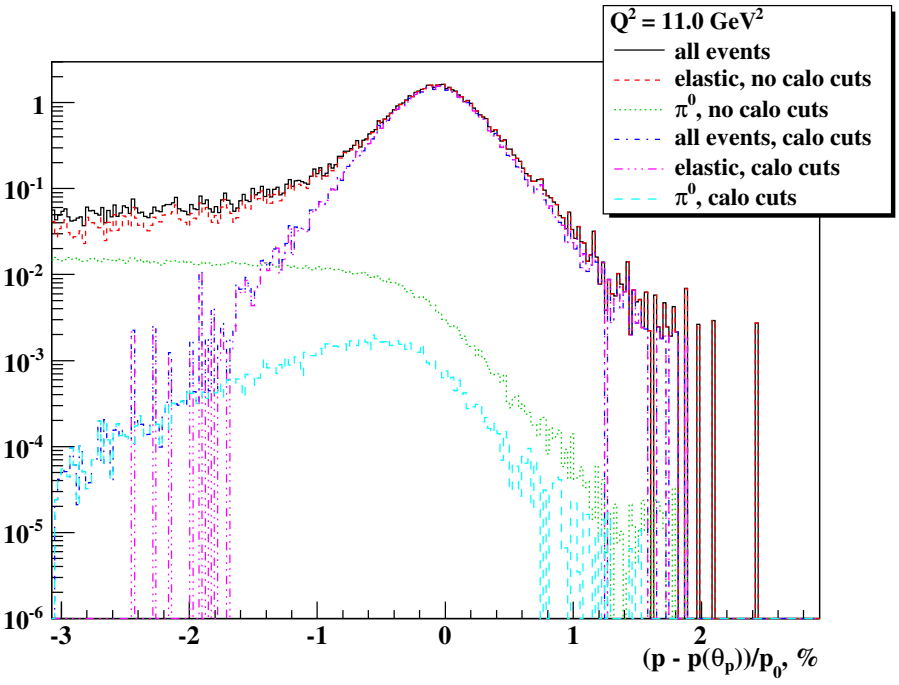

Figure 21: SIMC-estimated contributions from $ep \rightarrow ep$ and $\gamma p \rightarrow \pi^0 p$ at Q^2 = 11 GeV^2 with an 11 GeV beam.

A 30 cm liquid hydrogen target under standard operating conditions is a roughly 3.5% radiator. The rate of π^0 photoproduction is determined by the flux of hard-bremsstrahlung photons and the photoproduction cross section. Empirically, the cross section scales as s^{-7} for fixed θ_{CM} [75]. Thus, the JLab 12 GeV upgrade will result in much more favorable conditions from the point of view of the π^0 background than were experienced in GEp-III, in which the highest possible Q^2 was measured using a beam energy of only 5.7 GeV. With an 11 GeV beam, we have $(s(11\text{ GeV})/s(5.7\text{ GeV}))^{-7} = 0.01$. We have estimated the contamination of our elastic event sample from π^0 photoproduction using the standard Hall C Monte Carlo code SIMC. The calculation of the Bremsstrahlung flux in hydrogen and the photoproduction cross section with full s and θ_{CM} dependence in SIMC have been benchmarked against data from the GEp-III experiment, with excellent agreement between SIMC and estimates of the π^0 contamination obtained directly from the data. Figures 21, 22 and 23 show the results of the simulation for Q^2 = 11, 8.5 and 6 GeV^2.

The numerical results of the simulation for the π^0 contamination for different cut widths are shown in Tab. 1. Radiative effects tend to destroy the two-body kinematic correlations of the detected particles, reducing the effective elastic ep count rates after applying cuts compared to the rate of all events entering the experimental acceptance. Events in the radiative tail of elastic scattering cannot be separated from the π^0 background. As shown in Tab. 1, tight, 3σ cuts on the calorimeter position correlation and the proton angle-momentum correlation reduce the counting rate substantially, by 20-23% for our proposed kinematics. Although these cuts suppress the inelastic background to the 10^{-3} level or lower, their cost in efficiency is undesirable. Doubling the width of these cuts leads to efficiencies of 86-87%,

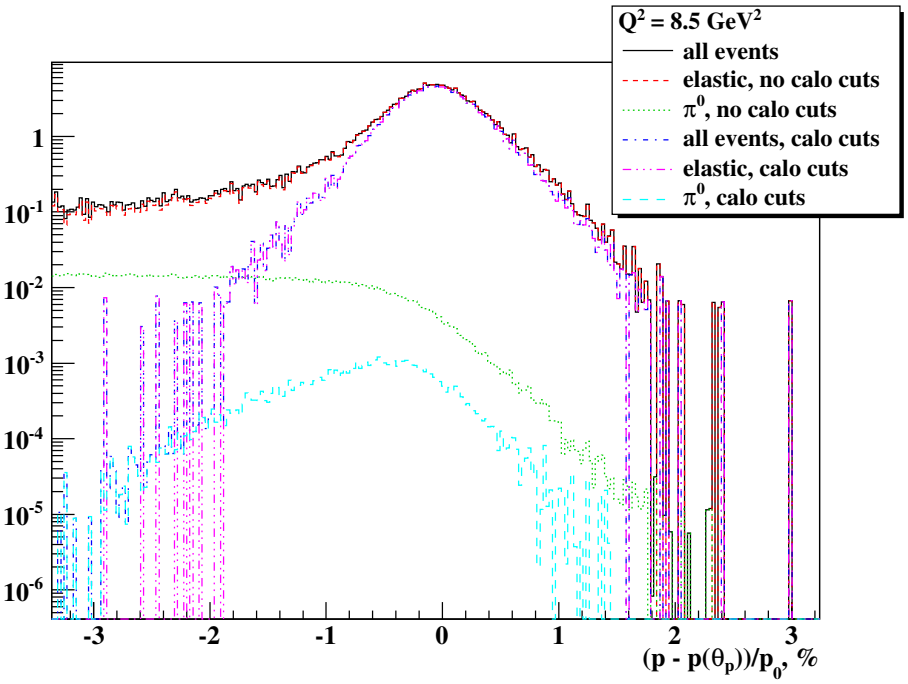

Figure 22: SIMC-estimated contributions from $ep \to ep$ and $\gamma p \to \pi^0 p$ at Q^2 = 8.5 GeV^2 with an 11 GeV beam.

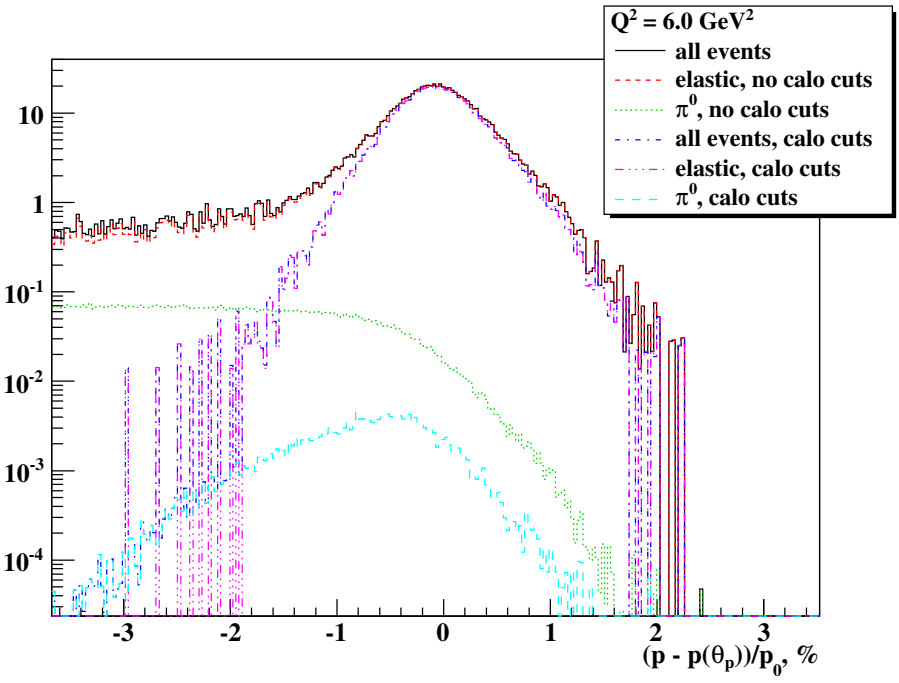

Figure 23: SIMC-estimated contributions from $ep \to ep$ and $\gamma p \to \pi^0 p$ at Q^2 = 6 GeV^2 with an 8.8 GeV beam.

but with a roughly 5-fold increase in the background contamination. Finally, removing all of the cuts leads to a substantial inelastic contamination. While the estimated background for the looser, 6σ cuts is still negligible from the point of view of the extraction of the ratio G_{Ep}/G_{Mp}, the considerable uncertainty in the prediction of the π^0 yield, which is based on the extrapolation of an empirical fit from the region of the fitted data to a largely unmeasured region in s, t space, underscores the fact that the coincident detection of the electron in this experiment is non-optional, a fact driven home by the GEp-III experiment (see Fig. 20), which could not have been successful without the use of BigCal[2].

Q^2, GeV^2	6.0	8.5	11.0
SIMC rate, mC^{-1}	761	184	60
bgnd. fraction, 3σ cuts	0.02 %	0.03%	0.15%
bgnd. fraction, 6 σ cuts	0.11 %	0.12%	0.61%
bgnd. fraction, no cuts	0.52%	2.16%	10.1%
cut efficiency, 3σ cuts	79.5%	78.1%	77.3%
cut efficiency, 6σ cuts	87.1%	86.3%	85.7%

Table 1: Comparison of the tradeoff between cut efficiency and π^0 background contamination in the proposed kinematics. The background fraction estimated by SIMC and the fraction of elastic events kept for cut widths of 3σ and 6σ applied to the calorimeter position correlation and the "missing momentum" $p_p - p_p(\theta_p)$. "SIMC rate" is the expected count rate per unit beam charge for a 30 cm target. The cut efficiency is less than 100% because the elasticity cuts suppress events affected by radiation from the incident and/or scattered electron.

The effect of the 1 cm-thick plastic S0 scintillator in GEp-III was to smear the angular resolution by a factor of approximately 2 in the non-dispersive plane, and by a factor of about 3 in the dispersive plane, where the difference in error magnification is a direct consequence of the HMS optics. Its effect on the momentum resolution, on the other hand, was small compared to the other sources of momentum resolution. The main effect of the degraded angular resolution in the elastic event selection is to smear the proton angle-momentum correlation, increasing the overlap between ep and π^0 events, and to smear the vertical coordinate difference at the calorimeter. The horizontal coordinate difference, on the other hand, is primarily determined by the HMS momentum resolution and the calorimeter coordinate resolution. The estimates given in Tab. 1 show that if necessary, we can safely trade the loss in resolution and the resulting wider cuts around the elastic peak for a lower accidental rate in the trigger, which will lead to a greater efficiency for recording elastic events, which is absolutely essential for achieving the proposed precision on G_{Ep}/G_{Mp}. If on the other hand the preferred solution of having no scintillators upstream of the HMS drift chambers proves feasible, the proposed experiment will have extremely clean elastic ep samples and negligible systematic uncertainty from backgrounds in the extraction of R.

Another source of background not mentioned here is quasielastic $Al(e, e'p)$ scattering

[2]Furthermore, the coincident detection of the electron and the selection of events based on their two-body kinematic correlations allows tight control of the (already small) radiative corrections to the polarization observables.

in the aluminum endcaps of the cryocell. Compared to the case of π^0 photoproduction, however, this background will be directly measured using the so-called "dummy" target. Modern cryotarget cells typically have very thin endcaps, and experience shows that even without using an explicit target vertex cut in the region overlapping with these endcaps, the aluminum background is strongly suppressed after applying all elasticity cuts, and if necessary, can be further suppressed using vertex cuts. The vertex resolution of the HMS is typically 1-2 mm in the horizontal direction perpendicular to its axis. The vertex resolution along the beamline then, is proportional to $1/\sin\theta_{HMS}$. In this experiment, the resolution of the vertex z coordinate will be conservatively 4-6 mm, For a 3σ cut of 1.2-1.8 cm at both ends of the target, the maximum reduction in effective target length would be about 10%. To reiterate, since our expectation from experience is that the aluminum background will be negligible after applying all cuts, we do not expect to cut out any of the target length in this experiment.

7.2 Calorimeter

Essential to this experiment is solid angle matching, which means that for each kinematics the solid angle of the electron detector must match the fixed solid angle of the proton detector, which is the HMS. For the Q^2 = 11 GeV^2 point, the electron scattering angle is larger than the proton recoil angle, and therefore the Jacobian for the electron is larger than 1, and hence the solid angle for the electron detector must be larger than that of the proton detector. For the lower Q^2 points the opposite is true and the electron detector solid angle is smaller than the proton one.

Of course, the situation here is exactly the same as for the GEp-III experiment in Hall C, for which a new large lead glass calorimeter array (BigCal) was constructed (see Fig. 24). This is the ideal detector for the electron in this experiment as well, as no modifications will be necessary. BigCal consists of 32 columns times 32 rows of 3.8×3.8 cm^2 bars of Protvino lead-glass blocks at the bottom, and 30 columns times 24 rows of 4.0×4.0 cm^2 bars from RCS (Yerevan blocks) placed on the top. The total frontal area is thus 2.63 m^2. In Fig. 25, the horizontal and vertical positions at the face of the calorimeter are plotted for each Q^2 point. The important thing for identifying elastic ep events is measuring the position at the calorimeter. This is used to determine the electron's angle and the ep angular correlation is part of the cut to identify elastic events. During GEp-III, the position resolution was estimated to be 8 mm.

7.2.1 Radiation Hardness of BigCal

BigCal was used in experiments 04-019 (GEp-2γ), 07-002 (WACS) and 04-108 (GEp-III) in Hall C between October 2007 and June 2008. Before the experiments, BigCal was roughly calibrated with cosmic muons. The first task with beam was commissioning BigCal using 1.06 GeV elastic electrons. To reduce the radiation damage, BigCal has an absorber consisting of four removable aluminum 1-inch thick plates in front of the lead-glass. In addition, a lucite plate (for checking the lead-glass PMTs with an LED system) and a 1/2 inch aluminum plate are permanently placed in front of the lead glass. Two absorber configurations were used during the calibration. The first used only one of the removable aluminum plates,

Figure 24: The BigCal Calorimeter.

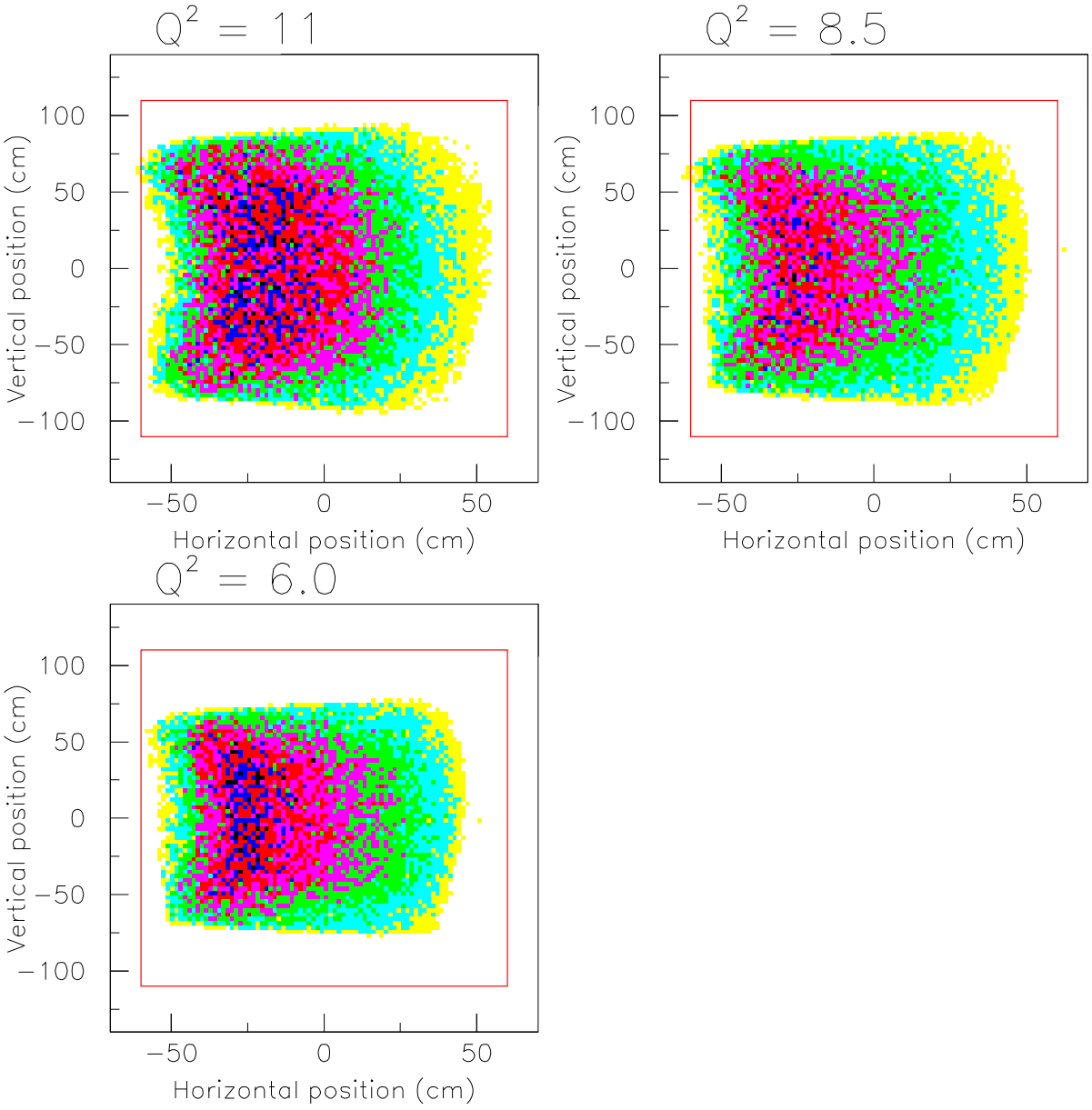

Figure 25: From a SIMC calculation, the expected distribution of elastic electrons at the calorimeter at distance of 10 m for Q^2 = 11 GeV^2 and 15 m for 8.5 and 6 GeV^2. The red box is the outer dimensions of the calorimeter.

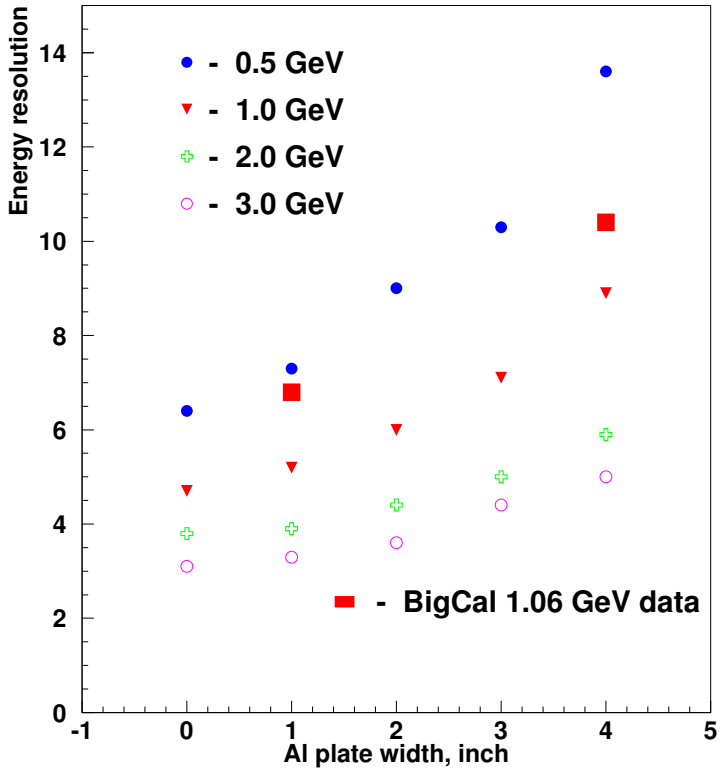

Figure 26: BigCal energy resolution (red solid boxes) obtained during commissioning using 1.06 GeV elastic electrons with two different absorber thicknesses (total thicknesses of 0.43 X_0 and 1.29 X_0, respectively) compared to Monte Carlo simulations for different energies as function of the additional Al absorber thickness.

and the second used all four plates, which together with the permanent aluminum plate results in thicknesses of 0.43 X_0 and 1.29 X_0, respectively. In Fig. 26, the measured energy resolutions are plotted as filled red squares at their given aluminum thickness. Also plotted in Fig. 26 are the predicted energy resolutions at different incident electron energies and aluminum thicknesses from a GEANT Monte Carlo simulation [76]. The experimentally achieved energy resolution differs by about 1-1.5% from the simulations and is among the best results obtained with this type of calorimeter especially given the additional absorber and the large number of channels. During E04-019 and GEp-III,which both measured the elastic ep reaction, the PMT gains in BigCal could be continually monitored using the predicted electron energy calculated from the measured angle and momentum of the proton detected in the HMS. Depending on the kinematics, the experiment could collect enough data in 1 to 8 hours to do a calibration. Due to the darkening of the lead-glass from radiation damage, there was an effective drop in the PMT gain and the energy resolution in BigCal gradually decreased ($i.e.$ increased width) thoughout the experiments. Most of the time, the PMT gain shifts were corrected in software, but when the shifts became large enough the HV of the PMTs was adjusted to increase the gain. By the end of the experiments the en-

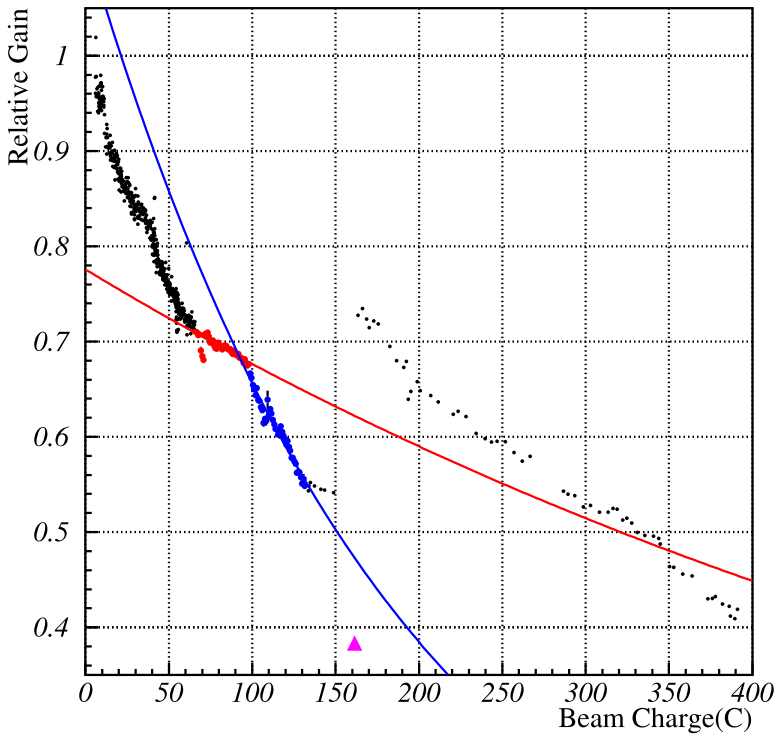

Figure 27: Mean gain of BigCal during the Gep-III experiments in Hall C (October 2007 - June 2008) as a function the accumulated beam charge in coulombs. The red (blue) points are during E04-019 with BigCal at angle of 44.9° (32°). The data points are fitted with ae^{-bC} (results given in Table 2). No data for the week-long WACS experiment (E07-002) is given except the last run (solid magenta triangle) just before the UV curing.

ergy resolution was $24\%/\sqrt{E}$, despite doing a partial UV curing of BigCal in January 2008 in the middle of the experiments. Figure 27 is a plot of the relative PMT gain versus the accumulated charge throughout all of the experiments. The relative gain, normalized to one at the beginning of the experiments, was obtained by averaging the gain of all the channels. For the relative gains shown in Fig. 27, when adjustments of the PMT HV were made the new gain was normalized to the previous value so that effective gain comparison can be done relative to the initial high voltages. A number of BigCal configuration changes were done during these experiments. For each new configuration, the effective gain of the PMTs would change (mainly due to dependence of the energy loss in the absorber on the electron energy) and a correction was applied at the beginning of each kinematics to ensure the continuity of the gain before and after the change of the kinematics. Generally, the different slopes in Fig. 27 correspond to different kinematics: different beam energy, angle and distance to the calorimeter.

After the E04-019 kinematics point with BigCal at 32° (blue points in Fig. 27), the Wide Angle Compton Scattering (WACS) experiment started. WACS used a 6% radiator in front of a 15 cm target liquid hydrogen target with BigCal placed at 11 m distance and an angle of 26°. Since normal WACS running did not have elastic ep events, the gain could not be monitored continuously. Only at the end of WACS were data taken for elastic ep events. The

Experiment	angle deg.	Dist. m	Target Length cm	Beam Energy GeV	Gain loss rate b	soft photon flux J/cm^2/C
E04-019	44.9	12	20	2.839	0.14 %/C	0.0039
E04-019	32.0	11.2	20	3.539	0.53 %/C	0.013
Gep-IV (Q^2 = 6)	20.1	15	30	8.8	0.75%/C	
Gep-IV (Q^2 = 8.5)	19.9	15	30	11.0	0.75%/C	
Gep-IV (Q^2 = 11)	25.5	10	30	11.0	1.4%/C	

Table 2: Gain loss per coulomb of beam estimated from the Fig. 27 for E04-019 at two angles. The GEANT prediction for the soft photon flux per coulomb for the two E04-019 points.

calibration point is the solid magenta triangle in Fig. 27 which shows a steep decline in the BigCal gain during the WACS experiment due to the forward BigCal angle and the radiator at the target.

After WACS the beam was down for a one month period, so it was decided to restore the lead-glass by using UV curing. Curing of the glass was performed with a specially constructed UV lamp that covered a quarter of the frontal calorimeter area. The lamp was moved at four different positions with an average time of 3 days per position. The effect of the UV curing corresponds to the jump in Fig. 27 between the red triangle (at 39%) indicating the gain before the curing and the next upper point (at 74%) after the curing. Fit with exponential function gives 1.24% per hour gain increase. Because of concerns about glass heating, there was a gap of 2" between the UV bulbs and the glass. During the curing it turned out that the glass temperature rose by only a few degrees, so the UV lamps could have been placed closer to the glass. Low power bulbs (14 W) were used so that damage to the PMTs that were left in place during the curing did not occur. After the GEp-III experiment, an additional UV lamp was built so that two UV lamps were available to cure the calorimeter for the SANE experiment with expected total curing time of 60 days per position. Constant check of the PMT performance showed no deviation from the normal gain, except some relaxation time was needed after long (several weeks) period of UV illumination.

To estimate the gain loss due to radiation damage to BigCal in this proposed experiment, two kinematic settings from E04-019 that had BigCal at 32° and 44.9° were studied. Both settings placed BigCal at about 11-12 m from the target. As shown in Fig. 27, the data points were fitted with the form: ae^{-bC} and the rate constant b is given in Table 2. Using GEANT simulations, the energy fluxes per coulomb through the front of the calorimeter have been estimated for both settings. As seen in Table 2, these numbers are roughly proportional to the gain loss rates estimated from Fig. 27. Thus, for the Gep-IV kinematics, one can predict the gain loss by assuming that it changes linearly with angle and target length and also accounting for changes in distance from the target. The predicted gain loss per coulomb is given in Table 2.

With a 75 μA beam current and a 50% running efficiency, one expects 3.25 C /day which corresponds to a 4.6% drop in gain per day for the Q^2 = 11 GeV^2 point. For the two lower Q^2 points, a 2.4% drop in gain per day is predicted.

We intend to build a permanent UV light box in front of the glass. The lucite plate and

1/2" thick aluminum plate will be removed. By placing the bulbs right next to the glass and increasing the power and density of the bulbs we expect to increase the UV flux by at least 5 times resulting in a gain increase rate of above 6%/hour. For the Q^2 = 11 GeV^2 point, this means in 5.5 hours about one week's worth of damage to the lead glass could be cured. This could be worked into the normal beam studies down periods. For the two lower Q^2 points, the lead-glass could be cured between changes of kinematics.

7.2.2 A Possible Alternative to BigCal - HYCAL

Interest in a general purpose radiation-hard medium-sized calorimeter that could be used in multiple experiments has been building at Jefferson Lab. The PrimEx collaboration has built a state-of-the-art hybrid calorimeter, HyCal, consisting of an inner section of 1152 $PbWO_4$ (PWO) scintillating crystals surrounded by 576 lead-glass bars arranged in a 1.18×1.18 m^2 grouping. HyCal was used in two experiments in Hall B with very good performance, namely, PrimEx-I in 2004 and most recently in PrimEx-II this year. The position resolution of the PWO section of HyCal was measured during PrimEx-I to be approximately 2 mm. Also, PWO is known to be about 100 times more resistant to radiation damage than lead-glass.

The PWO section of HyCal could be used in our proposed experiment. The detector would be placed approximately 4.5 m away from the target at an angle of about 23°. In this configuration the detector would be able to cover all three Q^2 points without having to move it. With a 2 mm position resolution, the electron angular resolution would be 0.4 mrad which is better than expected with the BigCal at 10 m. Given that PWO suffers less radiation damage by a factor of 100, the radiation dosage should only reduce the gain of PWO by about 8% over the course of the experiment. This means that thermal annealing or optical bleaching for recovery of the PWO would not be needed during the experiment.

7.3 Measurements

In Table 3, we present a summary of the kinematic points that have been chosen for GEp-IV. The three points chosen are justified as follows: the lowest point at a Q^2 of 6 GeV^2 will give a very small error bar in 10 days, and is the control point. The point at 8.5 GeV^2 is a strategic point: this is the highest point from GEp-III, and though the error bar was larger than expected, it may give indication that the ratio G_{Ep}/G_{Mp} is no longer decreasing linearly with a slope of -0.14/GeV^2, possibly the beginning of an evolution towards the expected pQCD behavior, namely $G_{Ep}/G_{Mp} \rightarrow constant$. The highest Q^2 is of course chosen to be the highest achievable with an existing magnetic spectrometer. We chose the HMS because it has $\sim$ twice the solid angle of the SHMS; furthermore the HMS has been studied extensively during and after GEp-III, particularly from the stand point of spin transport. The combination HMS-BigCal is fully understood and performing. There are several additional features that are worth noting:

- At the Q^2 values of 6 and 8.5 GeV^2, the electron scattering angle is approximately the same. Thus, no motion of BigCal is required between these two points.
- The beam energy values have been chosen to ensure that BigCal can be located on the beam side of the SHMS parked at its maximum angle of 40.3 degrees. The more

Q^2	E_e	θ_e	$E_{e'}$	θ_p	p_p	$d\sigma/d\Omega_e$	ϵ	χ	$\Delta\Omega_e$
GeV^2	GeV	deg	GeV	deg	GeV/c	cm^2/sr		deg	msr
6.0	8.8	20.1	5.60	28.5	4.03	3.2*10^{-35}	0.85	197.6	4.1
8.5	11.0	19.9	6.47	24.4	5.39	6.5*10^{-36}	0.83	261.2	5.3
11.0	11.0	25.5	5.14	19.2	6.74	0.9*10^{-36}	0.70	324.8	12.7

Table 3: The proposed kinematics. Assumed HMS spectrometer solid angle: 7 msr. Assumed beam characteristics: 75 μA, 85% polarization. Assumed target: 30 cm LH_2.

Q^2	E_e	COM	absolute $\Delta(G_{Ep}/G_{Mp})^*$	time
GeV^2	GeV			days
6.0	**8.8**	**3.9 $\times$ 10^{-3}**	**0.04**	**10**
8.5	**11.0**	**1.5 $\times$ 10^{-3}**	**0.10**	**20**
11.0	**11.0**	**1.1 $\times$ 10^{-3}**	**0.12**	**65**

Table 4: Absolute uncertainties (not including systematics), and times required. The assumed beam intensity and electron beam polarization are 75 μA and 0.85, respectively. The target length is 30 cm. The raw rates were estimated using the HMS-BigCal coincidence setup in SIMC with kinematic cuts. These raw rates were multiplied by an additional factor of 0.8 to account for deadtime, target boiling, and other possible losses. The total PAC time required for this experiment is 98 days (including three days for commissioning/optics/detector calibrations/etc..

favorable Jacobian (a by-product of the increase of the beam energy from 6 to 12 GeV) is small, allowing BigCal to be placed at distances from the target of at least 11 meters, which will minimize the lead-glass radiation exposure.

- Opting for the HMS has the additional advantage that the BigCal configuration can be the same as it was in GEp-III, with a height to width ratio of 1.68, which was optimized to match the HMS acceptance using a similar length LH_2 target, and is again ideal for this experiment.

Of particular importance in this experiment, as well as in GEp-III, is our ability to cleanly identify elastic ep scattering events; indeed, the fraction of elastic events compared to inelastic and other background events continues to decrease with increasing momentum transfer, but it increases with beam energy. In Table 4, we show projected uncertainties and beam times for all of the kinematics considered.

8 Summary

The total beam time requested for these three new data points is approximately 98 days, which includes an additional three days for commissioning/optics/detector calibrations/etc.. In Fig. 28, we summarize the currently available data for the proton form factor ratio, together with data from GEp-III, and the projected error bars for the approved E12-07-112

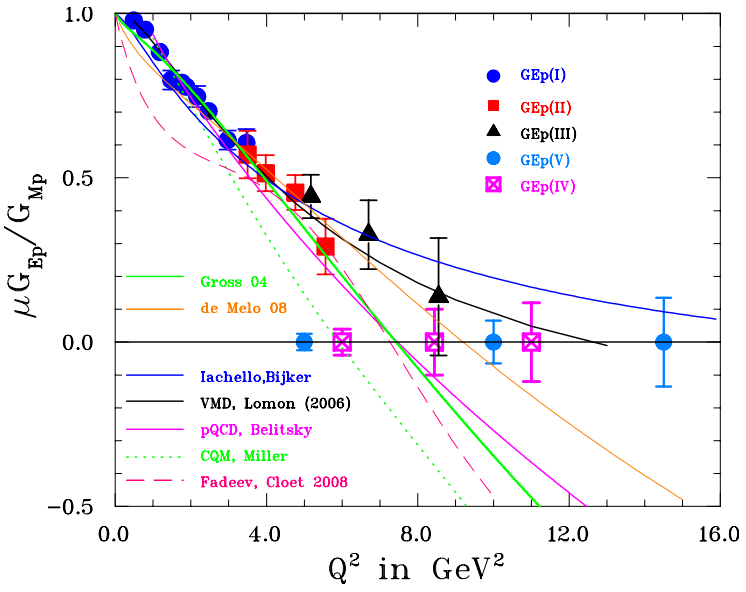

Figure 28: The points which will be measured following acceptance of this proposal are shown at 6, 8.5 and 11 GeV^2. The error bars are the statistical uncertainlies only. Systematic uncertainties originate mostly from the spin transport calculation, and are expected to be small by comparison. At 11 GeV^2, the relative background from π^0 photoproduction will be more than an order of magnitude smaller than in GEp-III, allowing the use of wider cuts on coplanarity and on the momentum difference, P_{miss}. The GEp-V points shown are at the Q^2 values of the proposal, with somewhat larger error bars as a result of the reduced beam time accorded by PAC36.

experiment in Hall A, and of course for this experiment. We also include the current projections from a range of theoretical models. In addition to the models discussed previously, we also show two phenomenological Vector Meson Dominance (VMD) inspired calculations ([74],[24]). It seems clear that data from this experiment will provide severe constraints on these and other models of this fundamental quantity.

We close by quoting the authors of the pCDR document for the 12 GeV JLab upgrade:

> *"The JLab 12 GeV Upgrade will support a great leap forward in our knowledge of hadron structure through major programs in three areas: nucleon form factors at large Q^2, valence quark structure, and deep exclusive scattering."*

We feel that the proposed experiment represents an opportunity which is in fact unique in the world to provide data on the proton form factor ratio at large Q^2, an essential ingredient in our understanding of the internal structure of hadrons.

References

[1] M. Göeckler *et al.*, Phys. Rev. D **71**, 034508 (2005).

[2] C. Alexandrou, G. Koutsou, J.W. Negele and A. Tsapalis, [arXiv: hep-lat/0605017], May 2006.

[3] R.C. Walker *et al.*, Phys. Rev. D **49**, 5671 (1994).

[4] L. Andivahis *et al.*, Phys. Rev. D **50**, 5491 (1994).

[5] M.E. Christy *et al.*, Phys. Rev. C **70**, 015206 (2004).

[6] I.A. Qattan *et al.*, Phys. Rev. Lett. **94**, 142301 (2005).

[7] M.K. Jones *et al.*, Phys. Rev. Lett. **84**, 1398 (2000).

[8] O. Gayou *et al.*, Phys. Rev. Lett. **88**, 092301 (2002).

[9] O. Gayou *et al.*, Phys. Rev. C **64**, 038202 (2001).

[10] V. Punjabi *et al.*, Phys. Rev. C **71** 055202 (2005).

[11] A. Afanasev *et al.*, Phys. Rev. D **64**, 113009 (2001).

[12] A.V. Afanasev, *et al.*, Phys. Rev. D **71**, 013008 (2005).

[13] P.G. Blunden, W. Melnitchouk, J.A. Tjon, Phys. Rev. Lett. **91**, 142304 (2003).

[14] Y.M. Bystritskiy, E.A. Kuraev and E. Tomasi-Gustafsson, Phys. Rev. C **75**, 015207 (2007).

[15] D. Borisyuk and A. Kobushkin, Phys. Rev. C **78**, 025208 (2008).

[16] N. Kivel and M. Vanderhaeghen, Phys. Rev. Lett. **103**, 092004, (2009).

[17] E. Brash, M. Jones, C.F. Perdrisat, V. Punjabi, E-04-108, "Measurement of G_E^p/G_M^p to 9 GeV^2 via recoil polarization" (2004).

[18] A.J.R. Puckett *et al.*, Phys. Rev. Lett. **104**, 242301, (2010).

[19] M. Meziane *et al.*, to be submitted to Phys. Rev. Lett. (2010).

[20] A.J.R. Puckett *et al.*, to be submitted for publication (2010).

[21] R. Gilman, L. Pentchev, C.F. Perdrisat, V. Punjabi, E-04-019, "Measurement of the two-photon exchange contribution in ep elastic scattering using recoil polarization" (2004).

[22] J. Arrington, proposal E-05-017, "A measurement of two-photon exchange in unpolarized elastic electron-proton scattering" (2005).

[23] C.F. Perdrisat, V. Punjabi, M. Vanderhaeghen, Prog. Part. Nucl. Phys. **59**, 694 (2007); arXiv:hep-ph/0612014.

[24] F. Iachello, A.D. Jackson and A. Landé, Phys. Lett. **B 43**, 191 (1973).

[25] M.F. Gari and W. Krümpelmann, Z. Phys. **A 322**, 689 (1985); M.F. Gari and W. Krümpelmann, Phys. Lett. **B 274**, 159 (1992); M.F. Gari and W. Krümpelmann, Phys. Lett. **B 282**, 483(E) (1992).

[26] S.J. Brodsky and G.R. Farrar, Phys. Rev. D **11**, 1309 (1975).

[27] E.L. Lomon, arXiv:nucl-th/0609020 (2006).

[28] R. Bijker and F. Iachello, Phys. Rev. C **69**, 068201 (2004).

[29] G. Höhler *et al.*, Nucl. Phys. B **114**, 505 (1976).

[30] P. Mergell, U.G. Meissner and D. Drechsel, Nucl. Phys. A **596**, 367 (1996).

[31] H.W. Hammer, U.G. Meissner and D. Drechsel, Phys. Lett. **B 385**, 343 (1996).

[32] M.A. Belushkin, H.W. Hammer and U.G. Meissner, Phys. Rev. C **75**, 035202 (2007).

[33] A. De Rujula, H. Georgi and S.L. Glashow, Phys. Rev. D **12**, 147 (1975); N. Isgur and G. Karl, Phys. Rev. D **18**, 4187 (1978); **19**, 2653 (1979); **20**, 1191 (1979); C. Hayne and N. Isgur, *ibid* **25**, 1944 (1982).

[34] P.L. Chung and F. Coester, Phys. Rev. D **44**, 229 (1991).

[35] M.R. Frank, B.K. Jennings and G.A. Miller, Phys. Rev. C **54**, 920 (1996).

[36] F. Schlumpf, Phys. Rev. D **47**, 4114 (1993).

[37] F. Cardarelli and S. Simula Phys. Rev. C **62**, 65201 (2000).

[38] E. Pace, G. Salme, F. Cardarelli and S. Simula, Nucl. Phys. A **666**, 33 (2000).

[39] M. De Sanctis, M.M. Giannini, L. Repetto and E. Santopinto, Phys. Rev. C **62**, 25208 (2000).

[40] S Boffi *et al.*, Eur. Phys. J. A **14**, 17 (2002); S. Boffi *et al.*, arXiv:hep-ph/0108271v1 (2001).

[41] G.A. Miller, Phys. Rev. C **68**, 022201(R) (2003).

[42] F. Gross and P. Agbakpe, Phys. Rev. C **73**, 015203 (2006).

[43] A. Kvinikhidze and G.A. Miller, Phys. Rev. C **73**, 065203 (2006).

[44] F. Gross, G. Ramalho and M.T. Peña, Phys. Rev. C **77**, 035203 (2008); arXiv:nucl-th/0606029 (2006).

[45] J.P.B. de Melo, T. Frederico, E. Pace, S. Pisano and G. Salme, arXiv:0804.1511 [hep-ph] (2008).

[46] G.P. Lepage and S.J. Brodsky, Phys. Rev. D **22**, 2157 (1980).

[47] S.J. Brodsky, arXiv:hep-ph/0208158v1 (2002).

[48] A.V. Belitsky, X. Ji and F. Yuan, arXiv:hep-ph/0212351 (2003).

[49] A.V. Radyushkin, Phys. Lett. **B 380**, 417 (1996); A.V. Radyushkin, Phys. Rev. D **58**, 114008 (1998).

[50] X. Ji, Phys. Rev. Lett. **78**, 610 (1997), Phys. Rev. D **55**, 7114 (1997).

[51] K. Goeke, M.V. Polyakov and M. Vanderhaeghen, Prog. Part. Nucl. Phys. **47**, 401 (2001).

[52] A.V. Afanasev, arXiv:hep-ph/9910565 (1999).

[53] M. Guidal, M.V. Polyakov, A.V. Radyushkin and M. Vanderhaeghen, Phys. Rev. D **72**, 054013 (2005).

[54] M. Diehl, T. Feldmann, R. Jakob and P. Kroll, Eur. Phys. J. C **39**, 1 (2005) [arXiv:hep-ph/0408173].

[55] M. Burkardt, Int. J. Mod. Phys. A **18**, 173 (2003).

[56] M. Diehl, Th. Feldmann, R. Jakob and P. Kroll, hep-ph/0408173 (2004).

[57] A.V. Belitsky, X. Ji and F. Yuan, Phys. Rev. D **69**, 074014 (2004).

[58] G.A. Miller, Phys. Rev. Lett. **99**, 112001 (2007); G.A. Miller and J. Arrington, Phys. Rev. C **78**, 032201 (2008).

[59] S. Venkat, J. Arrington, G. A. Miller and X. Zhan, arXiv:1010.3629 [nucl-th].

[60] C.E. Carlson and M. Vanderhaeghen, Phys. Rev. Lett. **100**, 032004 (2008) [arXiv:0710.0835 [hep-ph]].

[61] K.J. Wilson Phys. Rev. D **10**, 2445 (1974).

[62] C. Bernard *et al.*, Phys. Rev. D **61**, 111502R (2000); K. Orginos *et al.*, Phys. Rev. D **60**, 054503 (1999).

[63] F. Farchioni *et al.*, arXiv:hep-lat/0512017 (2006).

[64] R.G. Edwards *et al.*, LHPC Collaboration, arXiv:hep-lat/0610118 (2006).

[65] H.H. Matevosyan, G.A. Miller and A.W. Thomas, Phys. Rev. C **71**, 055204 (2005).

[66] G.A. Miller, Phys. Rev. C **66**, 032201 (2003).

[67] I.C. Cloët and C.D. Roberts, Proc. of Sc. LC2008:047 (2008); arXiv:0811.2018 [nucl-th] (2008); I.C. Cloët, G. Eichmann, B. El-Bennich, T. Klähn and C.D. Roberts, arXiv:0812.0416 [nucl-th] (2008).

[68] A.I. Akhiezer and M.P. Rekalo, Sov. J. Part. Nucl. **3**, 277 (1974).

[69] R. Arnold, C. Carlson and F. Gross, Phys. Rev. C **23**, 363 (1981).

[70] E. Aprile-Giboni *et al.*, Nucl. Instr. and Meth. **215**, 147 (1943).

[71] L.S. Azhgirey *et al.*, Nucl. Instr. and Meth. **A 538**, 431 (2005).

[72] N.E. Cheung *et al.*, Nucl. Instr. and Meth. **A 363**, 561 (1995).

[73] I.G. Alekseev *et al.*, Nucl. Instr. and Meth. **A 434**, 254 (1999).

[74] E.L. Lomon, Phys. Rev. C **64**, 035204 (2001).

[75] R.L. Anderson *et al.*, Phys. Rev. D **14**, 679 (1976).

[76] Monte Carlo calorimeter simulations, including Cherenkov photon propagagtion through lead-glass, developed by K. Shestermanov, IHEP, Protvino, Russia (2002).

[77] A. Gasparian, private communication.